

1 Visibility-derived aerosol optical depth over global land from 1980 to 2 2021

3 Hongfei Hao¹, Kaicun Wang², Chuanfeng Zhao³, Guocan Wu¹, Jing Li³

4 ¹Global Change and Earth System Science, Faculty of Geographical Science, Beijing Normal
5 University, Beijing 100875, China

6 ²Institute of Carbon Neutrality, Sino French Institute of Earth System Science, College Urban and
7 Environmental Sciences, Peking University, Beijing 100871, China

8 Email: kcwang@pku.edu.cn

9 ³Institute of Carbon Neutrality, Department of Atmospheric and Oceanic Sciences, School of
10 Physics, College Urban and Environmental Sciences, Peking University, Beijing 100871, China

11 Corresponding Author: Email: kcwang@pku.edu.cn

12 Abstract

13 Long-term and high spatial resolution aerosol optical depth (AOD) data are ~~essential~~necessary for
14 climate change detection and attribution. Global ground-based AOD observation stations are
15 sparsely distributed, and satellite AOD observations have a low temporal time-frequency, as well
16 low accuracy before 2000 over land. In this study, AOD ~~was-is~~ derived from hourly visibility
17 observations collected at more than 5000 meteorological stations ~~of the Automated Surface~~
18 ~~Observing System (ASOS)~~ over global land from 1980 to 2021. The AOD retrievals of the Moderate
19 Resolution Imaging Spectroradiometer (MODIS) onboard the Aqua Earth observation satellite ~~were~~
20 ~~are~~ used to train the machine learning ~~method~~model, and the ERA5 reanalysis boundary layer height
21 ~~was-is~~ used ~~to convert the surface visibility to AOD. Comparisons with independent dataset show~~
22 ~~that as input.~~ The predicted ~~result~~AOD has correlation coefficients of 0.54 and 0.55~~4~~ with Terra
23 MODIS satellite retrievals and AERONET ground observations ~~at daily time scale~~. The correlation
24 coefficients are higher at monthly and annual scales, which are 0.81~~08~~ and 0.61~~3~~ for the monthly
25 and 0.91~~06~~ and 0.65~~2~~ for the annual, compared with Terra MODIS and AERONET AOD,
26 respectively. The visibility-derived AOD at ~~ASOS~~ stations ~~scale is~~was gridded into a 0.5°-~~degree~~
27 ~~resolution grid~~ by ~~area-weighted~~ ordinary kriging interpolation. ~~Analysis of visibility-derived~~
28 ~~AOD indicates that for the global scale,~~ The mean ~~visibility-derived~~ AOD ~~of over the global~~ land
29 (-60°N-85°N), the Northern Hemisphere, and the Southern Hemisphere are 0.161, 0.158, and 0.173
30 ~~from 1980 to 2021~~, with a trend of -0.0026/10a, -0.0018/10a, and -0.0059/10a ~~from 1980 to 2021~~;
31 ~~respectively~~. For the regional scale, the mean ~~AOD (trends) of AOD from 1980 to 2021~~ are 0.145 (-
32 0.0041/10a), 0.139 (-0.0021/10a), 0.131 (-0.0009/10a), 0.153 (-0.0021/10a), 0.192 (-0.0100/10a),
33 0.275 (-0.0008/10a), 0.177 (-0.0096/10a), 0.127 (-0.0081/10a), 0.177 (-0.0003/10a), 0.222 (-
34 0.0000/10a), 0.232 (0.0071/10a), and 0.255 (0.0096/10a) in Eastern Europe, Western Europe,
35 Western North America, Eastern North America, Central South America, Western Africa, Southern
36 Africa, Australia, Southeast Asia, Northeast Asia, Eastern China, and India, ~~respectively~~. The
37 visibility-derived AOD at station and grid scales over global land from 1980 to 2021 are available

设置了格式: 上标

设置了格式: 上标

设置了格式: 上标

38 at National Tibetan Plateau / Third Pole Environment Data Center
39 (<https://doi.org/10.11888/Atmos.tpcd.300822>) (Hao et al., 2023).

40 How to cite. Hao, H., Wang, K., C. Zhao, Wu, G., J. Li (2023). Visibility-derived aerosol optical
41 depth over global land (1980-2021). National Tibetan Plateau / Third Pole Environment Data
42 Center. <https://doi.org/10.11888/Atmos.tpcd.300822>.

43 1 Introduction

44 Atmospheric aerosols are composed of solid and liquid particles suspended in the atmosphere.
45 ~~Aerosol particles are directly emitted into the atmosphere or formed through gas-particle~~
46 ~~transformation. Aerosol particles are primarily discharged from the Earth's surface broadly classified~~
47 ~~into natural and anthropogenic sources (Calvo et al., 2013). They possess, with~~ diverse shapes and
48 sizes (Fan et al., 2021), optical properties, and various components (Liao et al., 2015; Zhang et al.,
49 2020; Li et al., 2022), ~~such as inorganic salts, organic matter, metal elements and elemental carbon.~~
50 Most atmospheric aerosols are concentrated in the troposphere, especially in the boundary layer
51 (Liu et al., 2022), with a high concentration near emission sources (Kulmala et al., 2004), and a
52 small portion are distributed in the stratosphere, ~~with a sharp increase during large volcanic~~
53 ~~eruptions. Some aerosols from wildfires, volcanoes and sandstorms, play an important role in~~
54 ~~tropospheric aerosols. Studies have showed that 75% of volcanic eruptions inject volcanic aerosols~~
55 ~~and sulfur containing gases into the troposphere (Halmer et al., 2002), wildfire aerosols contribute~~
56 ~~up to approximately 35% of the fine particles in Europe (Barnaba et al., 2011), and dust aerosols are~~
57 ~~mainly concentrated in the middle and low troposphere (Filonchyk et al., 2018).~~ Atmospheric
58 aerosols severely impact the atmospheric environment and human health. They deteriorate air
59 quality, reduce visibility, and cause other environmental issues (Wang et al., 2012; Boers et al.,
60 2015). They ~~impair~~ affect human health or other organisms' conditions by increasing cardiovascular
61 and respiratory disease incidence and mortality rates (Chafe et al., 2014; Yang et al., 2022). The
62 Global Burden of Disease shows that global exposure to ambient PM_{2.5} resulted in 0.37 million
63 deaths and 9.9 million disability-adjusted life years (Chafe et al., 2014).

64
65 ~~In addition to environmental and health impacts, a~~ Aerosols are inextricably linked to climate change.
66 Atmospheric aerosols alter the Earth's energy budget and then affect the climate (Li et al., 2022).
67 They cool the surface and heat the atmosphere by scattering and absorbing solar radiation (Forster
68 et al., 2007; Chen et al., 2022). Aerosols, such as black carbon and brown carbon, also absorb solar
69 radiation (Bergstrom et al., 2007), heat the local atmosphere and suppress or invigorate convective
70 activities (Ramanathan et al., 2001; Sun and Zhao, 2020). Aerosols also alter the optical properties
71 and life span of clouds (Albrecht, 1989). Atmospheric aerosols strongly affect regional and global
72 short-term and long-term climates through direct and indirect effects (McNeill, 2017).

73 Tropospheric aerosols are considered as the second largest forcing factor for global climate change
74 (Li et al., 2022), and they reduce the warming due to greenhouse gases by -0.5°C (IPCC, 2021).
75 However, aerosols are also regarded as the largest contributor to quantifying the uncertainty of
76 present-day climate change (IPCC, 2021). ~~The uncertainties are caused by the deficiencies of the~~
77 ~~global descriptions of aerosol optical properties (such as scattering and absorption) and~~

78 ~~microphysical properties (such as size and component), and the impact on cloud and precipitation,~~
79 ~~further affecting the estimation of aerosol radiative forcing.~~The deficiency of the global descriptions
80 ~~of aerosol optical and microphysical properties is the primary reason for the uncertainty and the~~
81 ~~uncertainty also exists in climate models~~ (Lee et al., 2016; IPCC, 2021). Therefore, sufficient
82 aerosol observations are crucial. In aerosol measurements, aerosol optical depth (AOD) is often
83 used to describe its column properties, which represents the vertical integration of aerosol extinction
84 coefficients. AOD is an important physical quantity for estimating the content, atmospheric
85 pollution and climatology of aerosols (Zhang et al., 2020).

86 ~~AOD data usually from ground-based and satellite-borne remote sensing observation. They have~~
87 ~~both advantages and disadvantages. The measurements of aerosols are usually divided into in situ~~
88 ~~and remote sensing observations. In situ observations accurately measure the mass, number~~
89 ~~concentration, shapes, compositions and scattering and absorption of aerosols by directly sampling~~
90 ~~the air (Herich et al., 2008; Laj et al., 2020). Observations from airplanes and balloons can provide~~
91 ~~vertical structure (Ziemba et al., 2013). Because of its accuracy, in situ observation is often used as~~
92 ~~the benchmark for models and satellites, but its spatial representativeness is limited. Another method~~
93 ~~is~~ Ground-based lidar observation, which is an active remote sensing technology. Lidar generally
94 emits laser and receives backscattered signals to invert the extinction coefficient of aerosols at
95 different heights (Klett, 1985). By using the depolarization ratio, the type of aerosol, such as fine
96 particles or dust, can also be distinguished (Bescond et al., 2013). The AOD within a certain height
97 can be calculated by integrating the extinction coefficients; however, scattering signals are usually
98 not received near the ground, leading to blind spots (Singh et al., 2019). At present, there are many
99 ground-based lidar worldwide and regional networks, which provides important support ~~in the study~~
100 of vertical changes in aerosols, such as the NASA Micro-Pulse Lidar Network (MPLNET) in the
101 early 1990s (Welton et al., 2002), the European Aerosol Research Lidar Network (EARLINET)
102 since 2000 (Bösenberg and Matthias, 2003), the Latin American Lidar Network (LALINET) since
103 2013 (Guerrero-Rascado et al., 2016).

104
105 ~~The other two passive remote sensing observations of aerosol properties are ground-based and~~
106 ~~satellite borne remote sensing observations.~~ Ground-based remote sensing observations supply
107 aerosol loading data (such as AOD), by measuring the attenuation of radiation from the top of the
108 atmosphere to the surface (Holben et al., 1998). This type of observations mainly uses weather-
109 resistant automatic sun and sky scanning spectral radiometers to retrieve optical and microphysical
110 aerosol properties (Che et al., 2014). The Aerosol Robotic Network (AERONET) is a popular global
111 network composed of NASA and multiple international partners that provides high-quality and high-
112 frequency aerosol optical and microphysical properties under various geographical and
113 environmental conditions (Holben et al., 1998; Dubovik et al., 2000). The AERONET observations
114 are extensively used to validate ~~of~~ satellite remote sensing observations and model simulations, as
115 well as climatology study (Dubovik et al., 2002b). There are many regional networks of sun
116 photometers, such as the Maritime Aerosol Network (MAN), which use a handheld sun photometer
117 to collect data ~~over~~ the ocean and is merged into AERONET (Smirnov et al., 2009), the China
118 Aerosol Robot Sun Photometer Network (CARSONET) (Che et al., 2009), the Canadian sub-network
119 of AERONET (AEROCAN) (Bokoye et al., 2001), Aerosol characterization via Sun photometry:
120 Australian Network (AeroSpan) (Mukkavilli et al., 2019), and the sky radiometer network

121 (SKYNET) in Asia and Europe (Kim et al., 2004; Nakajima et al., 2020). Another very valuable
122 global network is the NOAA/ESRL Federated Aerosol Network (FAN), which uses integrated
123 nephelometers distinct from sun photometers, mainly located in ~~remote areas with less human~~
124 ~~activity impact~~, providing ~~background regionally representative~~ aerosol properties over 30 sites
125 (Andrews et al., 2019).

126 Satellite remote-sensing is a space-based method that can provide aerosol properties worldwide.
127 With the development of satellite remote sensing technology since 1970s, aerosol distributions can
128 be extracted with the advantage of sufficient real-time and global coverage from multiple satellite
129 sensors (Kaufman and Boucher, 2002; Anderson et al., 2005). The Advanced Very High Resolution
130 Radiometer (AVHRR) ~~was is~~ the earliest sensor used for retrieving AOD over ocean (Nagaraja Rao
131 et al., 1989). The Moderate Resolution Imaging Spectroradiometer (MODIS), on board the Terra
132 (launched in 1999) and Aqua (launched in 2002) satellites is a popular sensor with 36 channels,
133 which have been used for AOD retrieval over both ocean and land based on the Dark Target and the
134 Deep Blue algorithms (Remer et al., 2005; Levy et al., 2013). The latest MODIS AOD data version
135 is the Collection 6.1, which provides global AOD over 20 years (Wei et al., 2019a). There are also
136 many other satellite sensors that can be used to retrieve AOD, such as the Polarization and
137 Directionality of the Earth's Reflectances (POLDER) during 1996-1997, 2003 and 2004-2013
138 (Deuzé et al., 2000), Sea-viewing Wide Field-of-view Sensor (SeaWiFS) during 1997-2007
139 (O'Reilly et al., 1998), the Multi-angle Imaging Spectroradiometer (MISR) on Terra since 1999
140 (Diner et al., 1998). The Cloud-Aerosol Lidar with Orthogonal Polarization (CALIOP) has also
141 derived aerosols in the vertical direction since 2006 (Winker et al., 2009).

142 These measurements provide important data for studying the global and regional spatiotemporal
143 variabilities and climate effect of aerosols. However, ~~in situ and~~ ground-based remote sensing
144 observations only provide aerosol properties with low spatial coverage. There were only 1126
145 ground stations worldwide in 2002 and even fewer sites were available for climate analysis (Holben
146 et al., 1998; Chu et al., 2002), which limited aerosol climate research by spatial coverage (Bright
147 and Gueymard, 2019). Satellite remote sensing overcomes the limitations of spatial coverage. The
148 AVHRR has been used to retrieve AOD since 1980, but it is limited by a few channel number, low
149 spatial resolution, and insufficient validation through ground-based observations before 2000 (Hsu
150 et al., 2017). Many studies have only investigated the trends and distributions of aerosols after 2000
151 (Bösenberg and Matthias, 2003; Winker et al., 2013; Xia et al., 2016; Tian et al., 2023), because of
152 the lack of long-term and global cover AOD products, which is the bottleneck for aerosol climate
153 change detection and attributions.

154 To overcome these limitations and enrich aerosol data, alternative observation data could be utilized
155 to derive AOD. ~~For example, some studies used solar radiation data to infer AOD and analyze the~~
156 ~~characteristics of AOD in different regions (King et al., 1978; Vasilyev et al., 1995; Marenco et al.,~~
157 ~~1997; Qiu, 1997). There are also some studies deriving AOD based on empirical relationship~~
158 ~~between particle concentration and AOD (Xie et al., 2015; Li, 2020). These methods partially~~
159 ~~mitigate the scarcity of AOD data in spatial coverage, but it is also important to acknowledge the~~
160 ~~inherent limitation of long temporal coverage. Another more suitable alternative is a~~ atmospheric
161 horizontal visibility ~~is a suitable alternative (Wang et al., 2009; Zhang et al., 2020)~~, because it has
162 the advantages of the long-term records with a large number of stations worldwide.

163

164 Atmospheric visibility is a physical quantity that describes the transparency of the atmosphere
165 through manual and automatic observations, ~~and the automatic observations of visibility usually~~
166 ~~measure atmospheric extinction (scattering coefficient and transmissivity), including particle matter,~~
167 ~~water vapor, and gas molecules (Wang et al., 2009; Zhang et al., 2020), which makes it a favorable~~
168 ~~choice for inferring AOD.~~ Koschmieder (1924) first proposed the relationship between the
169 meteorological optical range and the total optical depth. Elterman (1970) further established a
170 formula between AOD and visibility by assuming an exponential decrease in aerosol concentration
171 with altitude, considering the extinction of molecules and ozone to analyze air pollution, which
172 called the Elterman model. Qiu and Lin (2001) corrected the Elterman model by considering the
173 influence of water vapor and used two water vapor pressure correction coefficients to retrieve AOD
174 of 16 stations in China in 1990. ~~Wang et al. (2009) analyzed the trend of AOD using visibility-based~~
175 ~~retrievals from 1973 to 2007 over land.~~ Lin et al. (2014) retrieved the AOD in eastern China in 2006
176 using visibility and aerosol vertical profiles provided by GEOS-Chem. Wu et al. (2014) and Zhang
177 et al. (2017) parameterized the constants in the Elterman model and use satellite retrieved AOD to
178 solve the parameters in the models at different stations, to retrieve the long-term AOD in China.

179 Zhang et al. (2020) reviewed the methods of visibility retrieval of AOD, indicating that visibility-
180 based retrieval of AOD can compensate for the shortcomings of long-term aerosol observation data.
181 Simultaneously, various parameters, such as station altitude, consistency of visibility data, water
182 vapor and aerosol vertical profiles (scale height), were discussed with modified suggestions
183 proposed. These studies have enriched AOD data regionally. ~~Due to the similar spatial distribution~~
184 ~~of the extinction coefficient and AOD, and the proportional relationship between the reciprocal of~~
185 ~~visibility and the extinction coefficient, Wang et al. (2009) analyzed the trend of AOD using~~
186 ~~visibility-based retrievals from 1973 to 2007 over land.~~ These studies have enriched aerosol data in
187 some extent. At present, there are very few studies on global visibility-retrieved AOD and to analyze
188 climatology of aerosols.

189 The two physical quantities of visibility and AOD have both connections and differences, making it
190 challenging to retrieve AOD from visibility. Visibility represents the maximum horizontal visible
191 distance near the surface, while AOD represents the total vertical attenuation of solar radiation by
192 aerosols. The visibility of automatic observation is dependent on the local horizontal atmospheric
193 extinction (NOAA et al., 1998). Visibility has not a simple linear relationship with meteorological
194 factors, ~~such as humidity and wind speed.~~ The vertical structure of aerosols is the greatest challenge
195 to obtain, as it is not a simple hypothetical curve in complex terrain and circulation conditions
196 (Zhang et al., 2020). These limitations make it more complex to derive AOD ~~over global land.~~
197 ~~However, previous studies have shown that surface observation data can establish a link with AOD,~~
198 ~~particularly at the regional scale.~~ Machine learning methods can effectively address complex
199 nonlinear relationships between variables and have been widely applied in remote sensing and
200 climate research fields. Li et al. (2021) used the random forest method to predict PM_{2.5} in Iraq and
201 Kuwait based on satellite AOD during 2001-2018. Kang et al. (2022) applied LightGBM and
202 random forest to estimate AOD over East Asia, and the results showed a consistency with
203 AERONET. Dong et al. (2023) derived aerosol single scattering albedo from visibility and satellite
204 AOD over 1000 global stations. Hu et al. (2019) used a deep learning method to retrieve horizontal
205 visibility from MODIS AOD. These studies have confirmed the ability of machine learning to

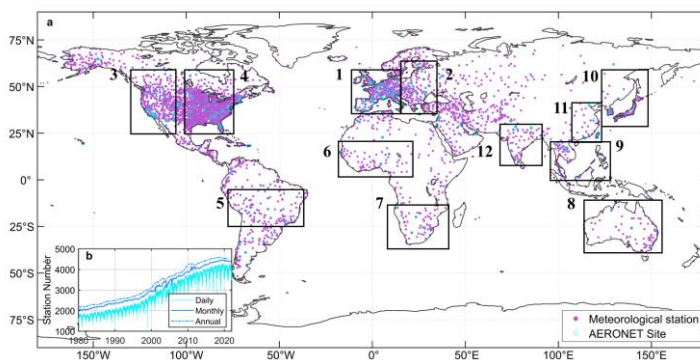
206 effectively solve complex relationships among variables. And ~~previous studies are mostly~~
207 ~~conducted at the regional or national scale, and few studies at the global scale.~~ Thus, it is feasible to
208 derive AOD from atmospheric visibility over global land by using the machine learning method.

209 In this study, we propose a machine learning method to derive AOD, where satellite AOD is the
210 target value, and ~~surface~~-visibility and other related meteorological variables are the predictors. We
211 explain the robustness of the model, validate ~~the accuracy of~~ the model's predictions using ground-
212 based AOD and ~~independent satellite retrieval~~ other observations, and analyze the ~~mean and trend~~
213 ~~climatology~~ of AOD across land and regions. Two datasets of long-term high-resolution AOD are
214 generated. The ~~Section 2 second part of this paper~~ introduces the data and method. The ~~Section 3 third~~
215 ~~part~~ is the evaluation and validation of the visibility-derived AOD, and the distribution and trends
216 are discussed at global and regional scales. The ~~Section 4 fourth part~~ presents the conclusions. This
217 study is dedicated to supporting the research of aerosols in climate change detection and attribution.

218 2 Data and method

219 2.1 Study area

220 The study area is global land. A total of 5032 ~~meteorological~~ stations ~~of the Automated Surface~~
221 ~~Observing System (ASOS), which is a joint surface weather observing network of the National~~
222 ~~Weather Service (NWS), the Federal Aviation Administration (FAA), and the Department of~~
223 ~~Defense (DOD) (NOAA et al., 1998). A total of and 573 stations of 395 AERONET sites~~ are selected
224 in this study, and shown in ~~Figure 1~~ ~~Figure 1 (a)~~. ~~Twelve 12~~ regions are selected for special analysis,
225 including Eastern Europe, Western Europe, Western North America, Eastern North America, Central
226 South America, Western Africa, Southern Africa, Australia, Southeast Asia, Northeast Asia, Eastern
227 China, and ~~Middle East~~ ~~India~~. The time range ~~in of~~ the study is from 1980 to 2021, during which the
228 records of ~~meteorological~~ stations are sufficient with a uniform spatial distribution. As shown in
229 ~~Figure 1~~ ~~Figure 1 (b)~~, the daily records have exceeded 1500 stations, and monthly and annual records
230 have exceeded 2000 during 1980-1990. After 2000, monthly records have reached 3000, which is
231 the foundation of gridding AOD.



232

233 **Figure 1** Study area (a) and the meteorological station number (b) with daily, monthly, and annual
234 records. The number of meteorological stations (filled circles) is 5032. The number of AERONET
235 sites (empty circles) is 3795. The box regions of labelled with number 1-12 are Eastern Europe,
236 Western Europe, Western North America, Eastern North America, Central South America, Western
237 Africa, Southern Africa, Australia, Southeast Asia, Northeast Asia, Eastern China, and [India](#).

238 2.2 Meteorological data

239 [The ground hourly data from 1980 to 2021 is collected from 5032 automated meteorological stations](#)
240 [of airports over land. Automated surface observations reduce errors associated with human](#)
241 [involvement in data collection, processing, and transmission. The data can be downloaded at](#)
242 <https://mesonet.agron.iastate.edu/ASOS>. The data is extracted from the Meteorological Terminal
243 [Aviation Routine Weather Report \(METAR\). The World Meteorological Organization \(WMO\) sets](#)
244 [guidelines for METAR reports, including report format, encoding, observation instruments and](#)
245 [methods used, data accuracy, and consistency. These requirements ensure consistency and](#)
246 [comparability of METAR reports globally. International regulations can be referenced at](#)
247 <https://community.wmo.int/en/implementation-areas-aeronautical-meteorology->
248 [programme. Among them, over 1,000 stations belong to the Automated Surface Observing System](#)
249 [\(ASOS\), and others are sourced from airport reports around the world.](#)

250 [The daily average visibility is calculated using harmonic mean. Experiments have found that](#)
251 [harmonic average visibility can better detect the weather phenomena than arithmetic average](#)
252 [visibility \(NOAA et al., 1998\). The visibility is calculated using the extinction coefficient, which is](#)
253 [directly proportional to the reciprocal of visibility \(Wang et al., 2009\). Harmonious average](#)
254 [visibility can capture the process of visibility decline more quickly. Therefore, daily visibility will](#)
255 [have greater representativeness:](#)

256 The hourly meteorological data from 1980 to 2021 are collected at 5032 globally distributed stations
257 (Figure 1) from the Automated Surface Observing System (ASOS), which is a joint effort of the
258 National Weather Service, the Federal Aviation Administration, and the Department of Defense,
259 downloaded at [https://www.ncei.noaa.gov/products/land-based-station/automated-surface-weather-](https://www.ncei.noaa.gov/products/land-based-station/automated-surface-weather-observing-systems)
260 [observing systems](#). From the 1960s to the 1970s, the Automated Meteorological Observing System
261 and Remote Automated Weather Observing System only reported objective elements, such as
262 temperature, dew point temperature, wind (speed and direction), and pressure. With technological
263 advancements, the ASOS was deployed and utilized in the 1980s. The automatic surface
264 observations reduced errors associated with human involvement in data acquisition, processing, and
265 transmission. Effective quality control methods are employed to ensure the quality of ASOS
266 products. ASOS provided hourly and even minutely ground automatic observations, primarily for
267 airports (NOAA et al., 1998; Dover et al., 2002). Atmospheric visibility of ASOS is measured by
268 the forward-scatter visibility sensor at 550 nm. The scattering angle of the sensor ranges from 0 to
269 45 degree, the sampling volume is 0.75 cubic feet and the response time is 20 seconds. The sensor
270 provides 1-minute average visibility with the day or night indication. Hourly visibility is calculated
271 based on the harmonic average of minutely visibility. Experiments have found that harmonic
272 average visibility can better detect the development of some weather phenomena than arithmetic
273 average visibility (NOAA et al., 1998). The sensor-measured visibility has a strong agreement with
274 the human observed during haze and homogeneous weather over a large area, even during periods

设置了格式: 默认段落字体, 字体: (默认) + 西文正文 (等线)

275 ~~when weather conditions are quite variable (NOAA et al., 1998). The same algorithm is used to~~
276 ~~calculate the daily, monthly, seasonally and yearly average visibility.~~

$$277 \quad V = n / \left(\frac{1}{V_1} + \frac{1}{V_2} + \dots + \frac{1}{V_n} \right) \quad \text{Eq. 1}$$

278 where V is the harmonic mean visibility, n = 24 for the daily meanvisibility, and V_1, V_2, \dots, V_n are
279 the individual hourly valuesvisibility.

280 ~~Visibility in METAR is reported in statute miles (SM). The reportable increments are: M1/4SM,~~
281 ~~1/4SM, 1/2SM, 3/4SM, 1SM, 1 1/4SM, 1 1/2SM, 1 3/4SM, 2SM, 2 1/2SM, 3SM, 4SM, 5SM, 6SM,~~
282 ~~7SM, 8SM, 9SM and 10SM. It is noted that visibility between zero and 1/4 statute mile is reported~~
283 ~~as M1/4SM8. Visibility values of exactly halfway between reportable values are rounded down.~~
284 ~~Visibility values of 10 miles or greater are reported as 10SM (NOAA et al., 1998).—~~

285 In addition to hourly visibility (VIS), other variables closely related to aerosol properties are selected,
286 including relative humidity (RH), dew point temperature (DT), temperature (TMP), wind speed
287 (WS) and sea-level pressure (SLP). Temperature affects atmospheric stability and the rate of
288 secondary particle formation, and humidity influences the size and hygroscopic growth, and wind
289 speed and pressure significantly impact the transport and deposition.~~In addition to hourly visibility~~
290 ~~(VIS), we also selected other automatically observed variables closely related to aerosol properties~~
291 ~~in this study. Because relative humidity influences the size and hygroscopic growth rate of particle~~
292 ~~matter, and wind speed and pressure significantly impact the transport and deposition of aerosols,~~
293 ~~relative humidity (RH), dew point temperature (DT), temperature (TMP), wind speed (WS) and sea-~~
294 ~~level pressure (SLP) are adopted. Additionally, sSky conditions (cloud amount) and hourly~~
295 ~~precipitation are also selected to remove the influence-records of extensive cloud cover and~~
296 ~~precipitation when deriving AOD.~~

297 We processed the data as follows. The records with missing values ~~were-are~~ eliminated (Husar et
298 al., 2000). When over 80% overcast or fog, the records of sky conditions ~~were-are~~ eliminated, though
299 such situations occur less than 1% of the time over land (Remer et al., 2008). The records with 1-
300 hour precipitation greater than 0.1 mm ~~were-are~~ eliminated. ~~The records with RH greater than or~~
301 ~~equal to 90% were eliminated.~~ We calculate the temperature dew point difference (dT). When the
302 RH is greater than 90%, it is impossible to distinguish whether it is fog or haze, or both, and even
303 precipitation. The records with RH greater than or equal to 90% are eliminated. When the RH is less
304 than 30%, the dilution effect of aerosols is very low or even negligible. When RH is between 30%
305 and 90%, visibility is converted to dry visibility (Yang et al., 2021c):—

$$306 \quad \text{VISD} = \text{VIS} / (0.26 + 0.4285 * \log(100 - \text{RH})) \quad \text{Eq. 2}$$

307 where VISD is the dry visibility.

308 Daily average of variables are calculated by at least 3 hourly records ~~with a harmonic mean for~~
309 ~~visibility (NOAA et al., 1998) and an arithmetic mean for the other variables.~~

310 **2.3 Boundary layer height**

311 The hourly boundary layer height (BLH) from 1980 to 2021 is available from the Fifth Generation
312 reanalysis of the European Medium-Range Weather Forecast Center (ERA5) with a resolution of

313 0.25° x 0.25° (<https://cds.climate.copernicus.eu>), which is the successor of ERA-Interim and has
314 undergone various improvements (Hersbach et al., 2020). The atmospheric boundary layer is the
315 layer closest to the Earth's surface and exhibits complex turbulence activities, and its height
316 undergoes significant diurnal variation. The effects of the boundary layer on aerosols are mainly
317 manifested in vertical distribution, concentration changes, transport, and deposition (Ackerman et
318 al., 1995). The characteristics and variations in the boundary layer play a crucial role in regulating
319 and adjusting the distribution of atmospheric aerosols. The boundary layer height serves as an
320 approximate measure of the scale height for aerosols (Zhang et al., 2020).

321 ~~Compared to observations of 300 stations over world from 2012 to 2019, the BLH of ERA5 was~~
322 ~~underestimated by 131.96m. Compared with the underestimated MERRA-2 (166.35m), JRA-55~~
323 ~~(351.49m), and NECP-2 (420.86m), the BLH of ERA5 was closest to the observations~~
324 ~~The BLH of ERA5 is considered to be the more promising dataset compared to the MERRA-2, JRA-55, and~~
325 ~~NCCEP-2 datasets~~ (Guo et al., 2021). The BLH hourly data is temporally and spatially matched with
326 the meteorological ASOS stations data before calculating the daily average.

327 ~~Because the inverse of visibility is proportional to the extinction coefficient and positively related~~
328 ~~to AOD (Wang et al., 2009), we calculated the reciprocal of visibility (VISI) and the reciprocal of~~
329 ~~dry visibility (VISDI). Due to the influence of boundary layer height on the vertical distribution of~~
330 ~~particles and the atmospheric aerosols are largely distributed in the boundary layer (Zhang et al.,~~
331 ~~2020), we calculated the product (VISDIB) of the reciprocal of dry visibility and BLH~~
332 ~~three variables (VISI, VISDI, VISDIB) are increased, shown in Eq. 3:~~ Therefore, the Predictor (Figure 2) is
333 composed of 11 variables (TMP, Td, dT, RH, SLP, WS, VIS, BLH, VISI, VISDI, and VISDIB).

334 2.4 MODIS AOD Products

335 Satellite daily AOD is available from the Moderate Resolution Imaging Spectroradiometer (MODIS)
336 Level 3 Collection 6.1 AOD products of the Aqua (MYD09CMA) satellite from 2002 to 2021 and
337 Terra (MOD09CMA) satellite from 2000 to 2021 with a spatial resolution of 0.05° x 0.05° at a
338 wavelength of 550 nm (<https://ladsweb.modaps.eosdis.nasa.gov>). MOD/MYD09 has a higher
339 spatial resolution than MOD/MYD08 (1° x 1°), which may result in a greater difference in AOD
340 values and reduce the proximity ratio to match the visibility-derived same AOD at station scale value.
341 Terra (passing approximately 10:30 am local time) and Aqua (passing approximately 1:30 pm local
342 time) were successfully launched in December 1999 and May 2002, respectively.

343 MODIS, carried on the Terra and Aqua satellites is a crucial instrument in the NASA Earth
344 Observing System program, which is designed to observe global biophysical processes
345 (Salomonson et al., 1987). The 2,330 km-wide swath of the orbit scan can cover the entire globe
346 every one to two days. MODIS has 36 channels and more spectral channels than previous satellite
347 sensors (such as AVHRR). The spectral range from 0.41 to 15- μ m representing three spatial
348 resolutions: 250 m (2 channels), 500 m (5 channels), and 1 km (29 channels). The aerosol retrieval
349 algorithms uses seven of these channels (0.47–2.13 μ m) to retrieve aerosol characteristics and uses
350 additional wavelengths in other parts of the spectrum to identify clouds and river sediments.
351 Therefore, it has the ability to characterize the spatial and temporal characteristics of the global
352 aerosol field.

353 The MODIS aerosol product actually takes use of different algorithms for deriving aerosols over
354 land and ocean. The Dark Target (DT) algorithm is applied to densely vegetated areas because the
355 surface reflectance over dark-target areas was lower in the visible channels and had nearly fixed

356 ratios with the surface reflectance in the shortwave and infrared channels (Levy et al., 2007; Levy
357 et al., 2013). The Deep Blue (DB) algorithm was originally applied to bright land surfaces (such as
358 deserts), and later extended to cover all cloud-free and snow-free land surfaces (Hsu et al., 2006;
359 Hsu et al., 2013). MODIS Collection 6.1 aerosol product was released in 2017, incorporating
360 significant improvements in radiometric calibration and aerosol retrieval algorithms.

361 The expected errors are $\pm (0.05 \pm 15\%)$ for the DT retrievals over land. Higher spatial coverage is
362 observed in August and September, reaching 86-88%. During December and January, due to the
363 presence of permanent ice and snow cover in high-latitude regions of the Northern Hemisphere, the
364 spatial coverage is 78-80%. Thus, challenges remain in retrieving AOD values in high-latitude
365 regions (Wei et al., 2019a). However, visibility observations are available in high-latitude regions,
366 thereby partially addressing the lack in these regions.

367 In this study, the Terra and Aqua MODIS AOD are temporally and spatially matched with the
368 meteorological ASOS stations. Aqua MODIS AOD is used as the Target, when training the model,
369 and Terra MODIS AOD is used in the evaluation and validation of the model results, as shown in
370 the flowchart (Figure 2Figure-2).

371 2.5 Ground-based AOD

372 Ground-based daily-15-minute AOD data are available from the Aerosol Robotic Network
373 (AERONET) Version 3.0 Level 2.0 product at 573-395 stations (Figure 1), which can be downloaded
374 from <https://aeronet.gsfc.nasa.gov>. The AERONET program is a federation of ground-based remote
375 sensing aerosol networks established by NASA and PHOTONS, including many subnetworks (such
376 as AeroSpan, AEROCAN, NEON, and CARSNET). The sun photometer (CE-318) measures
377 spectral sun and sky irradiance in the 340-1020 nm spectral range. When the aerosol loading is low,
378 the error is significant. When the AOD at 440 nm wavelength is less than 0.2, the error is 0.01,
379 which is equivalent to the error of the absorption band in the total optical depth (Dubovik et al.,
380 2002a). The total uncertainty in AOD under cloud-free conditions is less than ± 0.01 for wavelength
381 more than 440 nm, and ± 0.02 for wavelength less than 440 nm (Holben et al., 1998). AERONET
382 has three levels of AOD products: Level 1.0 (unscreened), Level 1.5 (cloud screened), and Level
383 2.0 (cloud screened and quality assured). Compared to Version 2, the Version 3 Level 2.0 database
384 has undergone further cloud screening and quality assurance, which is generated based on Level 1.5
385 data with pre- and post-calibration and temperature adjustment and is recommended for formal
386 scientific research (Giles et al., 2019). AERONET provides AOD products at wavelengths of 440,
387 675, 870, and 1020 nm. The AOD at 440nm and the Ångström index at 440-675nm are used for
388 AOD at 550 nm not provided by AERONET, as shown in Eq. 3, AERONET AOD, as the 'true'
389 value, is the average of at least two times within 1 hour (± 30 minutes) of Aqua transit time (Wei et
390 al., 2019a).

$$391 \tau_{550} = \tau_{440} \left(\frac{550}{440} \right)^{-\alpha} \quad \text{Eq. 3}$$

392 where τ_{440} and τ_{550} are the AOD at a wavelength of 440nm and 550 nm, and α is the Ångström
393 index.

394 The matching conditions between AERONET sites and meteorological stations are (1) a distance of
395 less than 0.5 ° (2) at least three years of observation. Finally, a total of 395 pairs were matched.

396 2.6 Decision Tree Regression

397 2.6.1 Feature selection

398 Although a multidimensional dataset can provide as much potential information as possible for
399 AOD, irrelevant and redundant variables can also introduce significant noise in the model and
400 reduce the model's accuracy and stability (Kang et al., 2021; Dong et al., 2023). Therefore, the F-
401 test is used to search for the optimal feature subset in the Predictor, aiming to eliminate irrelevant
402 or redundant features and select truly relevant features, which helps to simplify the model's input
403 and improve the model's prediction ability (Dhanya et al., 2020). The F-test is a statistical test that
404 gives an f-score($=-\log(p)$), p represents the degree to which the null hypothesis is not rejected) by
405 calculating the ratio of variances. In this study, we calculate the ratio of variance between the
406 Predictors and Target, and the features are ranked based on higher values of the f-score. A greater
407 value of f-score means that the distances between Predictors and Target are less and the relationship
408 is closer, thus, the feature is more important. We set $p=0.05$. When the score is less than $-\log(0.05)$,
409 the variable in the Predictors is not considered.

410 2.6.2 Data balance

411 When it is clear, the AOD value is small, the variability of AOD is small ($AOD < 0.5$), and the data is
412 concentrated near the mean value. When heavy pollution, the AOD value is large ($AOD > 0.5$). Compared
413 to clear sky, the AOD sequence will show "abnormal" large values with low frequency, which is the
414 imbalance of AOD data. Under good weather conditions (such as clear weather), the observed AOD
415 values are concentrated around the average value. Under bad weather conditions (such as heavy haze,
416 wildfires, sandstorms), the value values will vary significantly compared to the good weather conditions,
417 and the frequency of large AOD value is low. When the AOD time series is observed under both good
418 and bad weather conditions, the minority class is large AOD value. This is a phenomenon of data
419 imbalance. When dealing with imbalanced datasets, because of the tendency of machine learning
420 algorithms to perform better on the majority class and overlook the minority class, the model can be
421 underfit (Chuang and Huang, 2023). Data augmentation techniques are commonly employed to address
422 the issue in imbalance data, which applies a series of transformations or expansions to generate new
423 training data, thereby increasing the diversity and quantity of the training data.

424 The Adaptive Synthetic Sampling (ADASYN) is a data augmentation technique specifically designed to
425 address data imbalance problem (He et al., 2008; Mitra et al., 2023). It is an extension of the Synthetic
426 Minority Over-sampling Technique (SMOTE) algorithm (Fernández et al., 2018). The goal of ADASYN
427 is to generate synthetic sample data for the minority class to increase its representation in the dataset.
428 ADASYN, which adaptively adjusts the generation ratio of synthetic samples based on the density
429 distribution of sample data, improves the dataset balance and enhances the performance of machine
430 learning models in dealing with imbalanced data.

431 The processing of imbalanced data includes (1) AOD sequences are classified into three types based on
432 percentile (0-1%, 2% -98%, 99%), (2) When the mean of the third type of AOD is greater than 5 times
433 the standard bias of the second type, it is considered an imbalanced sequence. These data, with a total
434 amount less than 5% of the sample, are imbalanced data, and (3) Then synthetic samples are generated
435 with the upper limit 10% of the samples.

436 2.6.3 Decision Tree Regression Model

437 The decision tree is a machine learning algorithm based on a tree-like structure used to solve
 438 classification and regression problems. We adopt the CART algorithm to construct a regression tree by
 439 analyzing the mapping relationship between object attributes (Predictors) and object values (Target). The
 440 internal nodes have binary tree structures with feature values of "yes" and "no". In addition, each leaf
 441 node represents a specific output for a feature space. The advantages of the regression tree include the
 442 ability to handle continuous features and the ease of understanding the generated tree structure (Teixeira,
 443 2004; Steinberg and Colla, 2009). Before training the tree model, the variables (Input) are normalized to
 444 improve model performance, and after prediction, the results are obtained by denormalization. The 10-
 445 fold cross-validation method is employed to improve the generalization ability of the model (Browne,
 446 2000).

447 The core problems of the regression tree need to be solved are to find the optimal split variable and
 448 optimal split point. The optimal split point of Predictors is determined by the minimum MSE, which in
 449 turn determines the optimal tree structure. We set $Y = [y_1, y_2, \dots, y_N]$ as the Target. We set $X =$
 450 $[x_1, x_2, \dots, x_N]$ as the Predictors, $x_i = (x_i^1, x_i^2, \dots, x_i^n), i = 1, 2, 3, \dots, N$, where n is the feature number, and
 451 N is the length of sample. We set a training dataset as $D = [(x_1, y_1), (x_2, y_2), \dots, (x_N, y_N)]$.

452 A regression tree corresponds to a split in the feature space and the output values on the split domains.
 453 Assuming that the input space has been divided into M domains $[R_1, R_2, \dots, R_M]$ and there is a fixed
 454 output value on each R_M domain, the regression tree model can be represented as follows:

$$455 \quad f(x) = \sum_{m=1}^M c_m I(x \in R_m), m = 1, 2, \dots, M \quad \text{Eq. 4}$$

456 where I is the indicator function (Eq. 85):

$$457 \quad I = \begin{cases} \mathbf{1}, & x \in R_m \\ \mathbf{0}, & x \notin R_m \end{cases} \quad \text{Eq. 5}$$

458 When the partition of the input space is determined, the square error can be used to represent the
 459 prediction error of the regression tree for the training data, and the minimizing square error is used to
 460 solve the optimal output value on each domain. The optimal value (\widehat{c}_m) on a domain is the mean of the
 461 outputs corresponding to all input, namely:

$$462 \quad \widehat{c}_m = \text{ave}(y_i | x_i \in R_m) \quad \text{Eq. 6}$$

463 A heuristic method is used to split the feature space in CART. After each split, all values of all features
 464 in the current set are examined individually, and the optimal one is selected as the split point based on
 465 the principle of minimum sum of the square errors. The specific step is described as follows: for the
 466 training dataset D , we recursively divide each region into two sub domains and calculate the output
 467 values of each sub domain; then, construct a binary decision tree. For example, split variable is x^j and
 468 split point is s . Then, in the domain $R_1(j, s) = [x | x^j \leq s]$ and domain $R_2(j, s) = [x | x^j > s]$, we can
 469 solve the loss function $L(j, s)$ to find the optimal j and s .

$$470 \quad L(j, s) = \sum_{x_i \in R_1(j, s)} (y_i - c_1)^2 + \sum_{x_i \in R_2(j, s)} (y_i - c_2)^2 \quad \text{Eq. 7}$$

471 When $L(j, s)$ is the smallest, x^j is the optimal split variable and s is the optimal split point for the
 472 x^j .

$$\min_{j,s} \left[\min_{c_1} \sum_{x_i \in R_1(j,s)} (y_i - c_1)^2 + \min_{c_2} \sum_{x_i \in R_2(j,s)} (y_i - c_2)^2 \right] \quad \text{Eq. 8}$$

We use the optimal split variable x^j and the optimal split point s to split the feature space and calculate the corresponding output value.

$$\hat{c}_1 = \text{ave}(y_i | x_i \in R_1(j,s)), \quad \hat{c}_2 = \text{ave}(y_i | x_i \in R_2(j,s)) \quad \text{Eq. 9}$$

We traverse all input variables to find the optimal split variable x^j , forming a pair (j,s) . Divide the input space into two regions accordingly. Next, repeat the above process for each region until the stop condition is met. The regression tree is generated.

Therefore, the regression tree model $f(x)$ can be represented as follows:

$$f(x) = \sum_{m=1}^M \hat{c}_m I(x \in R_m), \quad m = 1, 2, \dots, M \quad \text{Eq. 10}$$

2.7 Gridding method

Kriging is a regression algorithm to model and predict (interpolate) random processes/fields based on the covariance function, which is widely used in geo-statistics (Pebesma, 2004). Ordinary Kriging is the earliest and most extensively studied form of Kriging. It is a linear estimation system applicable to any intrinsic stationary random field that satisfies the assumption of isotropy. The two key parameters of Ordinary Kriging are the semi-variogram function and the weight factors (Goovaerts, 2000). It has been widely applied in fields, such as climatology, environmental science, and agriculture (Lapen and Hayhoe, 2003; Chen et al., 2010), due to high accuracy, stability, and insensitivity to data shape and distribution. This study utilizes area-weighted ordinary kriging algorithm to estimate the unknown values of AOD at specific locations to generate gridded AOD. The longitude range is between ~~-179.5480~~° E and 180 °E, the latitude range is between -60 °N and 85 °N, and the spatial resolution is 0.5 °*0.5 °.

2.8 Evaluation metrics

Evaluation metrics, including Root Mean Squared Error (RMSE), Mean Absolute Error (MAE) and Pearson Correlation Coefficient (R), are used to measure the performance and accuracy of the model and gridded results.

$$RMSE = \sqrt{\frac{1}{n} \sum_{i=1}^n (y_i - \hat{y}_i)^2} \quad \text{Eq. 11}$$

$$MAE = \frac{1}{n} \sum_{i=1}^n |y_i - \hat{y}_i| \quad \text{Eq. 12}$$

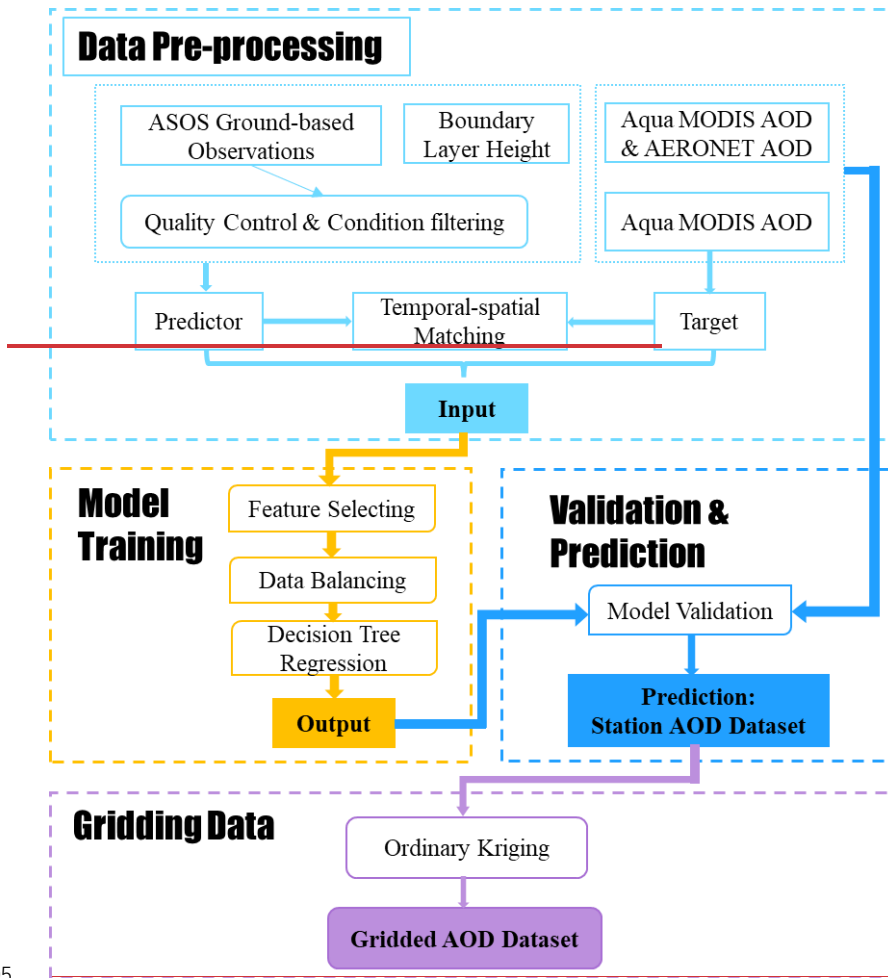
$$R = \frac{\sum_{i=1}^n (y_i - \bar{y})(\hat{y}_i - \bar{\hat{y}})}{\sqrt{(\sum_{i=1}^n (y_i - \bar{y})^2) (\sum_{i=1}^n (\hat{y}_i - \bar{\hat{y}})^2)}} \quad \text{Eq. 13}$$

where y_i and \bar{y} are the predicted value and the average of the predicted values. \hat{y}_i and $\bar{\hat{y}}$ are the target and the average of the target. $i = 1, 2, \dots, n$. n is the length of sample.

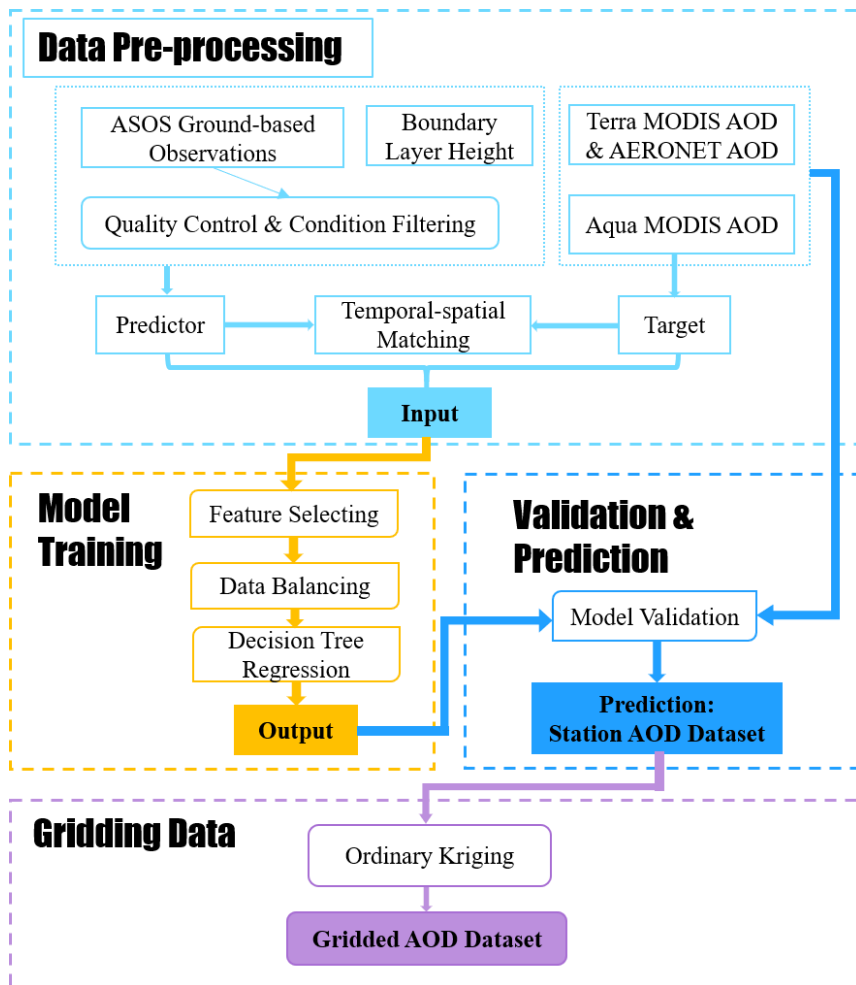
The expected error (EE) is used to evaluate the AOD derived from visibility.

$$EE = \pm(0.05 + 0.15 * \tau_{target}) \quad \text{Eq. 14}$$

where τ_{target} is AERONET AOD or Terra MODIS AOD at 550nm.



505



506

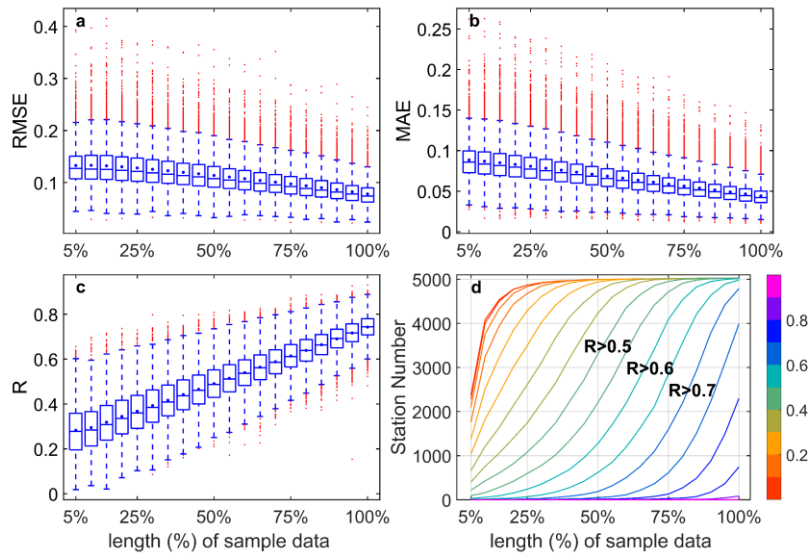
507 **Figure 2** Flowchart for deriving aerosol optical depth (AOD).

508 2.9 Workflow

509 **Figure 2** is the summarized flowchart and provides an overview of the structure of this
 510 study, which involves four main parts: (1) data preprocessing, (2) model training, (3) validation and
 511 prediction, and (4) data gridding.

512 3 Results and discussion

513 3.1 Dependence of model performance on training data length ~~Examination of the model~~ 514 ~~performance~~



515

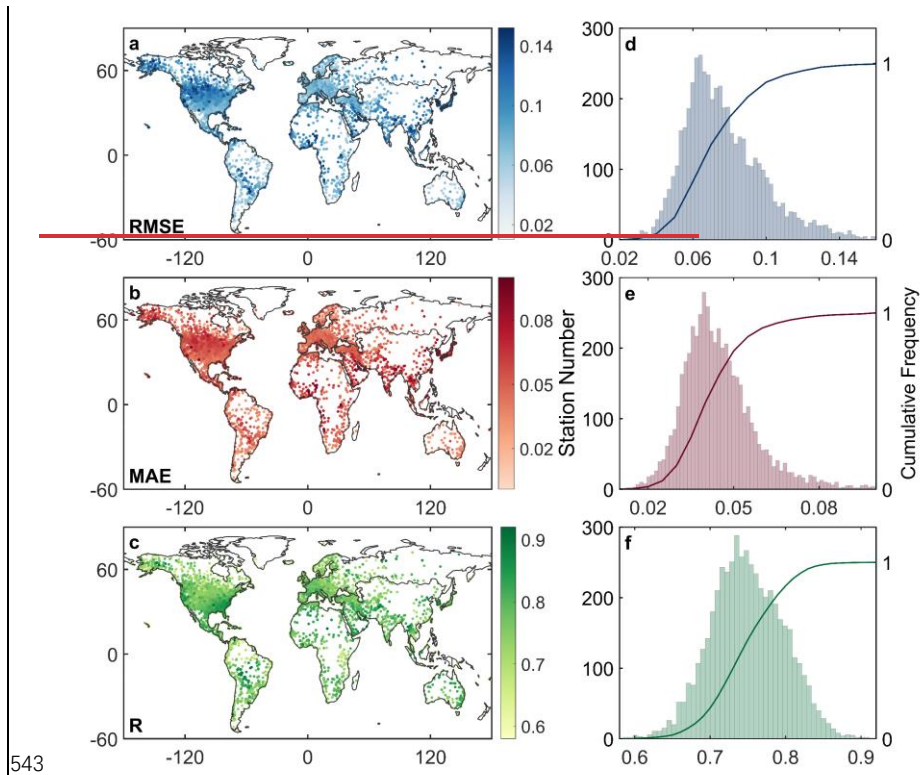
516 **Figure 3** Boxplots of root mean squared error (RMSE) (a), mean absolute error (MAE) (b),
 517 and correlation coefficient (R) (c) between predicted values and target using different lengths of
 518 sample data (5% interval) as the training dataset, and the correlation coefficient curve (d) of the
 519 station number in the different lengths of sample data.

520 We build the models using different lengths of sample data (5% to 100%, with a 5% interval) by random
 521 allocation without overlap and evaluate the predictive performance of each model. **Figure 3**
 522 depicts RMSE(a), MAE(b), and R (c) between the predicted values and target based on the training data
 523 of 5% to 100% sample data at a station. As the volume of the training data increases, the RMSE and
 524 MAE decrease, and the correlation coefficient increases. Compared to 5% of the sample data, the result
 525 of 100% sample data shows a decrease in RMSE by 41.1%, a decrease in MAE by 50.1%, and an increase
 526 in R by 162.3%. The relationship between the length of sample data and the model's performance is
 527 positive for each station. **Figure 3** (d) shows that R of approximately 70% of stations is greater
 528 than 0.5 at 50% of the sample data, while at 75%, the R of approximately 80% of stations is greater than
 529 0.6. When 100% of the sample data is used as sample data, the R of approximately 80% of stations is
 530 greater than 0.75, and the R of about 97% is greater than 0.7. This finding indicates that the predictive
 531 capability and robustness of the model increase as the amount of training data increases. It may be
 532 attributed to the model's ability to capture more complex patterns and relationships among the input by
 533 multi-year data.

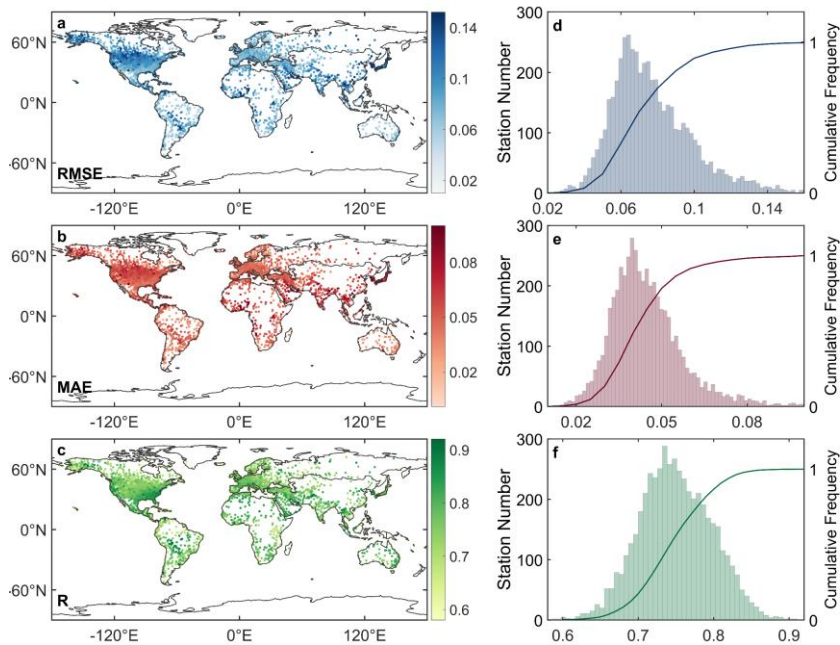
534 **3.2 Evaluation of model error training**

535 ~~The more sample data input, the better the model performs. Therefore, 100% of the sample data were~~
 536 ~~used as training data.~~ **Figure 4** shows the spatial distribution (a-c) and frequency and cumulative
 537 frequency (d-e) of RMSE, MAE, and R of all stations. The mean values of RMSE, MAE, and R are 0.078,
 538 0.044, and 0.750, respectively. The RMSE of 93% stations is less than 0.11, the MAE of 91% is less than

539 0.06, and the R of 88% is greater than 0.7. The R values in Africa, Asia, Europe, North America, Oceania,
540 and South America are 0.763, 0.758, 0.736, 0.750, 0.759, and 0.738, respectively. Although the RMSE
541 and MAE of a few stations are high in America and Asia, the R is still high (>0.6). Therefore, the results
542 of the model's errors demonstrate that the model performs well on almost all stations.



543

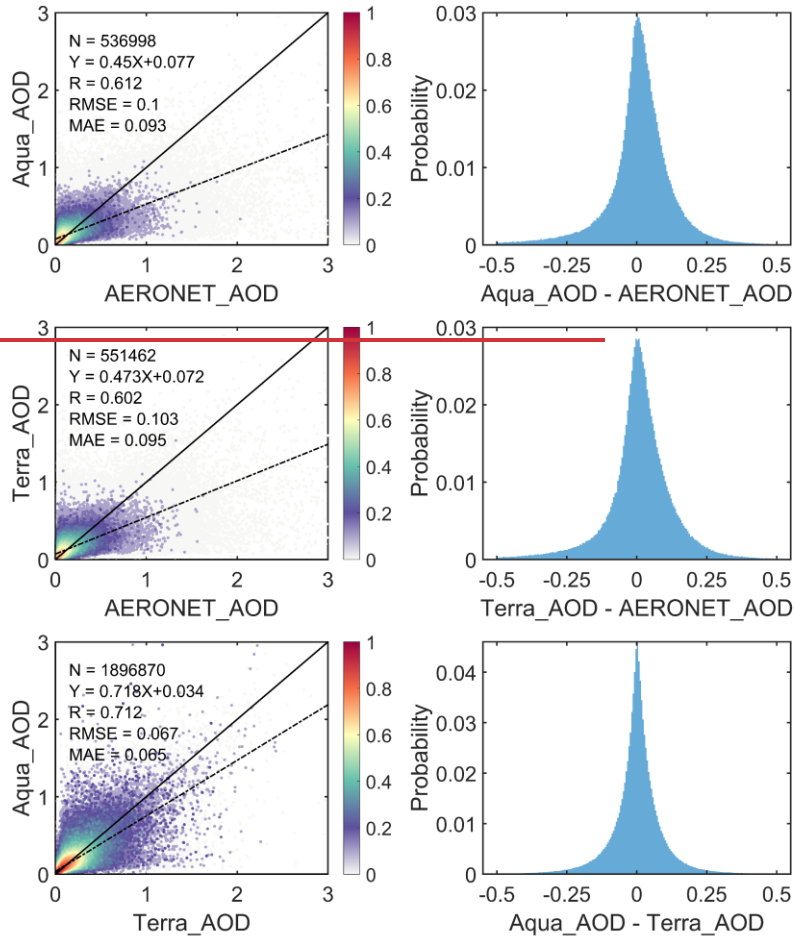


544

545 **Figure 4** Figure 4 Spatial distribution (a-c) of root mean squared error (RMSE), mean absolute
 546 error (MAE), and correlation coefficient(R) between the model's result and target with 100% sample
 547 data. Station number (bar) and cumulative frequency (curve) (d-e) of RMSE, MAE, and R.

548 **3.3 Validation and comparison with MODIS and AERONET AOD** Validation of derived AOD
 549 against MODIS and AERONET AOD

550 First, the relationship among daily MODIS and AERONET AOD is evaluated. Figure 5 presents the
 551 scatter density plots (the left column) and bias probability distribution (the right column) among daily
 552 Aqua, Terra and AERONET AOD. The R, RMSE, and MAE of 536,998 data couples between Aqua AOD
 553 and AERONET AOD are 0.612, 0.1, and 0.093, respectively. Then, 86.8% of the data have a bias within
 554 ± 0.093 . The R, RMSE, and MAE of 551,462 data couples between Terra AOD and AERONET AOD are
 555 0.602, 0.103, and 0.095, respectively. Then 86% of the data have a bias within ± 0.095 . The R, RMSE,
 556 and MAE of 1,896,870 data couples between Aqua AOD and Terra AOD are 0.712, 0.067, and 0.065,
 557 respectively, and the bias is within ± 0.065 for 92% of the data. On the global scale, the AOD retrieved
 558 by satellites may be overestimated at low AOD levels and underestimated at high AOD levels compared
 559 to AERONET AOD. Approximately 86% of the bias values are less than the MAEs. Terra and Aqua have
 560 good consistency, although one is for morning transit and the other is for afternoon transit. Finally, 92%
 561 of the data bias are less than the MAEs. Thus, there is good consistency among them on the daily scale.



562

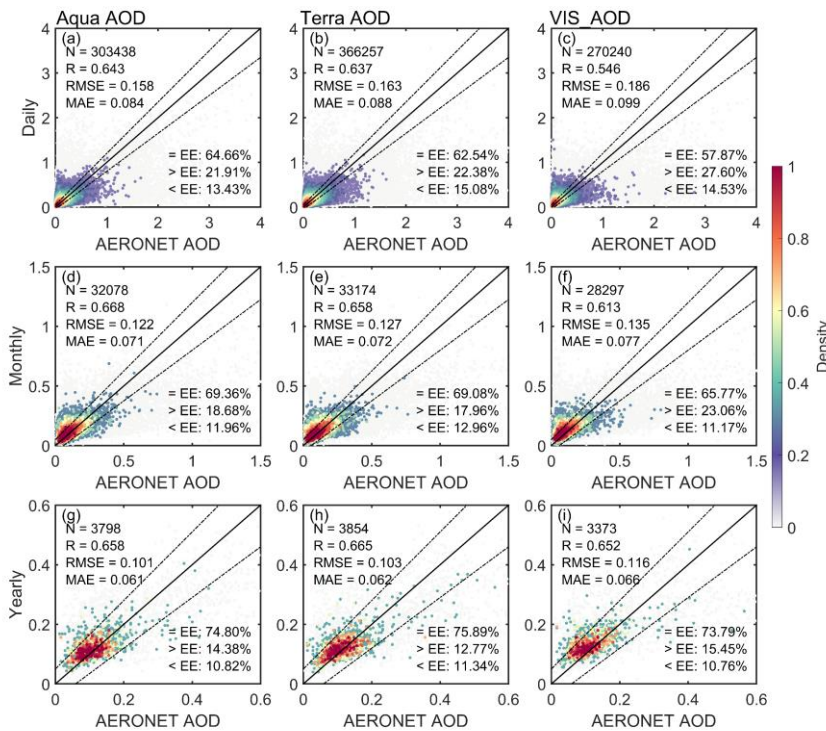
563 **Figure 5** Scatter density plots and bias probability between Aqua AOD, Terra AOD and AERONET
 564 AOD at a daily scale. The solid black line represents the 1:1 line and the dashed black line is the
 565 linear regression line.

566 **3.3.1 Validation over global land**

567 To validate the model's predictive ability, the visibility-derived AOD (for short, VIS_AOD) is compared
 568 with Aqua, Terra and AERONET AOD at 550nm for the global scale ~~other observed data for daily,~~
 569 ~~monthly, and yearly scales of Aqua, Terra and AERONET AOD.~~ Among them, Aqua AOD has been used
 570 as training data, which is not independent. Terra AOD and AERONET AOD have not been used as
 571 training data and can be regarded as independent data.

572 First, the relationship among daily MODIS and AERONET AOD is evaluated. Figure 5 shows the scatter
 573 density plots between AERONET AOD and Aqua AOD (a, d, g) and Terra AOD (b, e, h). The R values

574 with Aqua AOD and Terra AOD are 0.643 and 0.637 on the daily scale, and 0.668 and 0.658 on the
 575 monthly scale, 0.658 and 0.665 on the yearly scale. The RMSE with Aqua AOD and Terra AOD are 0.158
 576 and 0.163 on the daily scale, and 0.122 and 0.127 on the monthly scale, 0.101 and 0.103 on the yearly
 577 scale. The MAE values with Aqua AOD and Terra AOD are 0.084 and 0.088 on the daily scale, and 0.071
 578 and 0.072 on the monthly scale, 0.061 and 0.062 on the yearly scale. The percentages of sample point
 579 falling within the EE envelopes are 64.66% and 62.54% on the daily scale, and 69.36% and 69.08% on
 580 the monthly scale, 74.80% and 75.89% on the yearly scale.



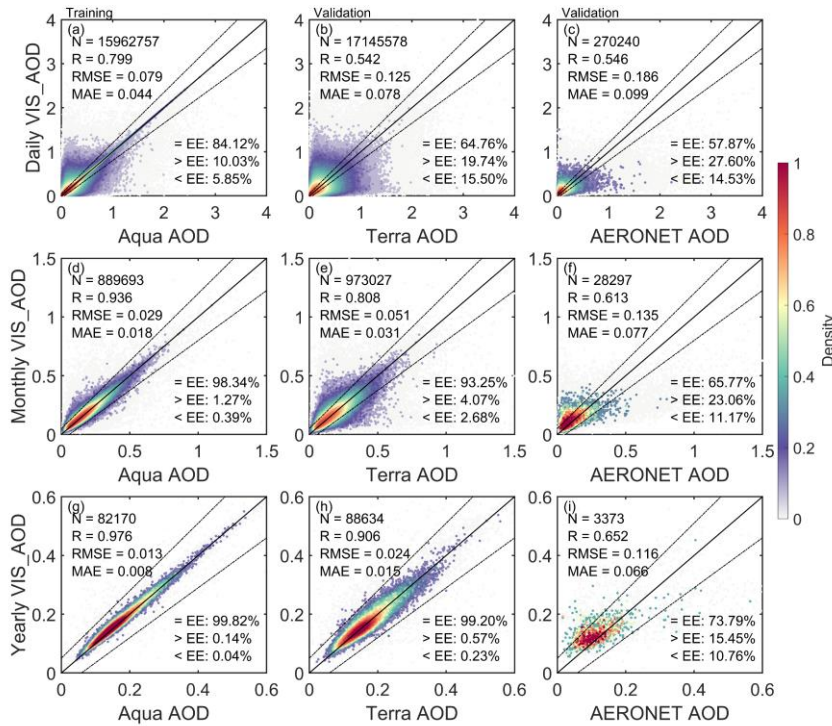
581
 582 **Figure 5** Scatter density plots between AERONET AOD (550nm) and Aqua MODIS AOD, Terra MODIS
 583 AOD and VIS AOD at the daily (a-c), monthly (d-f) and yearly (g-i) scale. The solid black line represents
 584 the 1:1 line and the dashed lines represents expected error (EE) envelopes. The sample size (N),
 585 correlation coefficient (R), mean absolute error (MAE), and root mean square error (RMSE) are given.
 586 ‘=EE’, ‘>EE’, and ‘< EE’ represent the percentages (%) of retrievals falling within, above, and below
 587 the EE, respectively. The matching time for Aqua AOD and VIS AOD with AERONET AOD is 13.30
 588 (± 30 minutes) at local time, and the matching time between Terra AOD and AERONET AOD is 10.30
 589 (± 30 minutes) at local time.

590 Figure 6 shows the scatter density plots and the EEs between VIS AOD and Aqua AOD, Terra AOD,
 591 and AERONET AOD. Aqua AOD is not an independent validation, and Terra and AERONET AOD are
 592 independent validation. For the daily scale, the R, RMSE and MAE of between VIS AOD and Aqua
 593 AOD (15,962,757 pairs data) is 0.799, 0.079 and 0.044, respectively. The percentage of sample point

594 falling within the EE envelopes is 84.12% on the global scale (Figure 6 a). The R between VIS_AOD
595 and Terra AOD (17,145,578 pairs data) is 0.542, with a RMSE of 0.125 and MAE of 0.078. The
596 percentage falling within the EE envelopes is 64.76% (Figure 6 b). The R between VIS_AOD and
597 AERONET AOD (270,240 pairs data) at 397 sites is 0.546, with a RMSE of 0.186 and MAE of 0.099.
598 The percentage falling within the EE envelopes is 57.87% (Figure 6 c).

599 For the monthly and annual scales, RMSE and MAE show a significant decrease between VIS_AOD and
600 Aqua, Terra, and AERONET AOD, and R and percentages falling within EE show a significant increase
601 in Figure 6 (d-i). The monthly RMSEs are 0.029, 0.051, and 0.135, the monthly MAEs are 0.018, 0.031,
602 and 0.077, and the R values are 0.936, 0.808, and 0.613, respectively. The percentages falling within the
603 EE envelopes are 98.34%, 93.25%, and 65.77%. The RMSEs at the annual scale are 0.013, 0.024, and
604 0.116, the MAEs are 0.008, 0.015, and 0.066, and the R values are 0.976, 0.906, and 0.652, respectively.
605 The percentages falling within the EE envelopes are 99.82%, 99.20%, and 73.79%. The percentage
606 falling within the EE envelopes against AERONET is smaller than that against Terra, which may be
607 related to the elevation of AERONET sites, the distance between AERONET and meteorological stations,
608 and observed time. The results highlighted above demonstrate a clear improvement in performance on
609 the monthly and annual scales compared to the daily scale (Schutgens et al., 2017), which provided a
610 foundation for the gridded dataset.

611 On the daily, monthly, and annual scales, compared with AERONET AOD, the correlation coefficients,
612 RMSE, MAE, and percentages falling within the expected error of VIS_AOD and MODIS AOD are very
613 close. Since the time of AERONET AOD and VIS_AOD overlaps before 2000, it indicates that
614 VIS_AOD also has the same accuracy.



615

616 **Figure 6** Scatter density plots between predicted AOD (VIS AOD) and Aqua MODIS AOD, Terra
 617 MODIS AOD and AERONET AOD at the daily (a-c), monthly (d-f) and yearly (g-i) scale. The solid
 618 black line represents the 1:1 line and the dashed lines represents expected error (EE) envelopes. The
 619 sample size (N), correlation coefficient (R), mean absolute error (MAE), and root mean square error
 620 (RMSE) are given. ‘=EE’, ‘>EE’, and ‘< EE’ represent the percentages (%) of retrievals falling within,
 621 above, and below the EE, respectively. Note Aqua AOD is not an independent validation for predicted
 622 results, while Terra and AERONET are independent validation.

623 **3.3.2 Validation over regions**

624 Aerosol loading exhibits spatial variability. Evaluation metrics for the relationships between
 625 visibility-derived AOD and AERONET AOD and Terra AOD for each region are listed in Table 1.
 626 Over Europe and North America, the results are similar to those of Terra and AERONET, with a
 627 large number of data pairs, greater than 10^5 (AERONET) and greater than 10^7 except for Eastern
 628 Europe (Terra) on the daily scale. Approximately 63% -70% fall within the EE envelopes. The
 629 RMSE is approximately 0.1100, except for western North America, the MAE is approximately
 630 0.0700, with a correlation coefficient between 0.44 and 0.54.

631 Over Central South America, South Africa, and Australia, data pairs are about 10^{3-4} (AERONET)
 632 and 10^6 (Terra) on the daily scale. 52-60% fall within the EE envelopes compared to AERONET,
 633 and 58-67% compared to Terra. The RMSE is 0.03-0.05 compared to Terra, and 0.11-0.17 compared
 634 to AERONET. The correlation coefficient ranges from 0.4 to 0.74, with the highest correlation

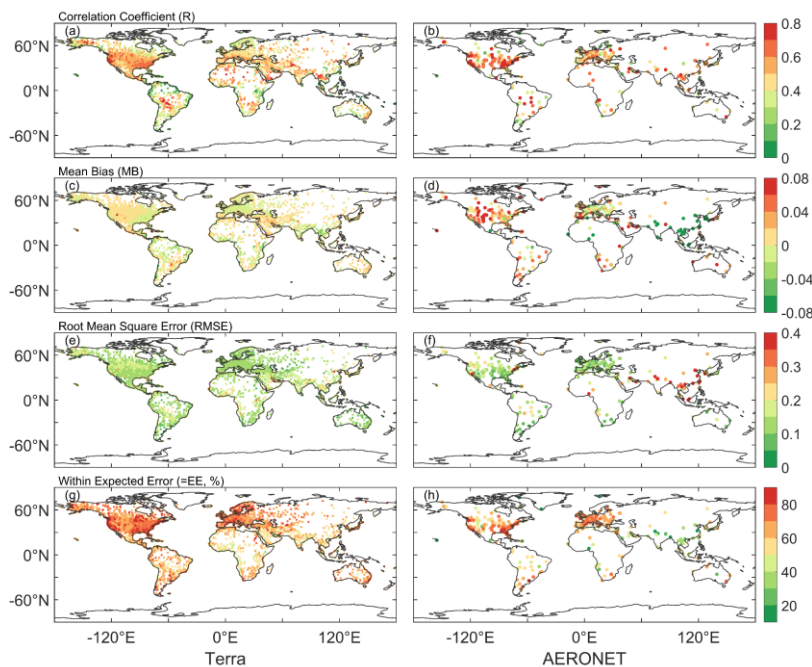
635 coefficient in South America at 0.740.
636 In Asia, India, and West Africa, the data pairs are only approximately 10^4 (AERONET). 32% to 50%
637 fall within the EE envelopes compared to AERONET, the RMSE ranges from 0.2 to 0.5, and the
638 MAE ranges from 0.11 to 0.36. 51 to 58%, compared to Terra, fall within the EE envelopes, the
639 RMSE is around 0.16, and the MAE is around 0.11. Compared to AERONET, in these high aerosol
640 loading regions, RMSE and MAE increase, and the percentages falling within the EE envelopes
641 decrease, but the correlation coefficients do not significantly decrease.
642 Compared to Terra AOD, 55% -67% of data falls within the EE envelopes on the daily scale, 87% -
643 96% on the monthly scale, and over 97% on the yearly scale. Compared to AERONET AOD, 32-
644 68% of data falls within the EE envelopes, 24% -84% on the monthly scale, and 15% -97% on the
645 yearly scale. On both monthly and yearly scales, all metrics have shown a significant increase in
646 performance when compared to Terra. However, compared to AERONET, not all metrics increase
647 in some regions due to limited data pairs, such as West Africa, Northeast Asia, and India, which may
648 be due to the spatial differences between AERONET sites and meteorological stations.
649 Overall, the AOD from visibility is more effective in regions such as Europe and North America,
650 which may also be related to the better performance of the MODIS DT algorithm in vegetation-
651 covered regions. In high aerosol load areas affected by deserts, such as Africa and Asia, the AOD of
652 visibility inversion needs to be improved.
653 **3.3.3 Validation at a site scale**
654 Sites, especially AERONET, are not completely uniform across the world or in any region, and
655 different stations have different sample sizes, which may lead to a certain uncertainty. Therefore,
656 further analysis was conducted on the spatial distribution of different evaluation metrics. Figure 7
657 shows the validation and comparison of daily VIS_AOD against Terra and AERONET AOD at a
658 site scale.
659 Compared to Terra daily AOD, the R of 67% stations is greater than 0.4, the mean bias of 83% is

Table 1 Evaluation metrics for the relationships between visibility-derived AOD and AERONET AOD and Terra AOD for each region.

Region	—	N			R			RMSE			MAE			Within EE (%)		
		daily	monthly	yearly	daily	monthly	yearly	daily	monthly	yearly	daily	monthly	yearly	daily	monthly	yearly
<i>Eastern Europe</i>	<i>AERONET</i>	21724	2317	271	0.463	0.493	0.653	0.1069	0.0647	0.0326	0.0714	0.0442	0.0263	65.69	83.77	97.42
	<i>TERRA</i>	661630	36435	3278	0.464	0.665	0.790	0.1095	0.0471	0.0214	0.0726	0.0286	0.0122	66.07	94.71	99.18
<i>Western Europe</i>	<i>AERONET</i>	53043	6033	697	0.445	0.487	0.344	0.1089	0.0716	0.0513	0.0711	0.0474	0.0347	64.40	79.21	89.10
	<i>TERRA</i>	1778013	104620	9166	0.467	0.763	0.811	0.1096	0.0391	0.0210	0.0712	0.0268	0.0124	66.99	95.42	99.40
<i>Western North America</i>	<i>AERONET</i>	33859	2948	334	0.503	0.484	0.509	0.1465	0.0949	0.0566	0.0747	0.0597	0.0419	63.58	67.37	81.14
	<i>TERRA</i>	1725226	82734	7201	0.542	0.765	0.906	0.1144	0.0465	0.0180	0.0671	0.0267	0.0125	69.48	94.42	99.61
<i>Eastern North America</i>	<i>AERONET</i>	47407	5359	608	0.527	0.526	0.559	0.1135	0.0824	0.0436	0.0657	0.0472	0.0331	67.52	77.78	87.50
	<i>TERRA</i>	6280277	359520	31343	0.515	0.799	0.847	0.1159	0.0435	0.0165	0.0726	0.0275	0.0111	66.70	94.94	99.80
<i>Central South America</i>	<i>AERONET</i>	10911	1176	149	0.740	0.811	0.866	0.1735	0.1272	0.1060	0.1021	0.0904	0.0688	52.40	47.96	67.79
	<i>TERRA</i>	444780	26362	2410	0.545	0.820	0.776	0.1447	0.0591	0.0369	0.0909	0.0396	0.0219	58.48	89.29	97.39
<i>Southern Africa</i>	<i>AERONET</i>	4255	309	38	0.423	0.480	0.630	0.1553	0.1128	0.0705	0.1033	0.0805	0.0525	52.08	59.55	78.95
	<i>TERRA</i>	216239	11304	1118	0.518	0.821	0.870	0.1258	0.0511	0.0296	0.0836	0.0340	0.0191	60.64	91.70	98.21
<i>Australia</i>	<i>AERONET</i>	6426	516	63	0.488	0.654	0.363	0.1094	0.0827	0.0725	0.0711	0.0620	0.0563	59.96	59.88	71.43
	<i>TERRA</i>	284693	14588	1286	0.398	0.784	0.831	0.1091	0.0363	0.0188	0.0666	0.0261	0.0143	67.01	94.65	99.38
<i>Western Africa</i>	<i>AERONET</i>	2205	205	34	0.553	0.594	0.762	0.3180	0.2873	0.3357	0.2082	0.2029	0.2587	37.96	40.00	23.53
	<i>TERRA</i>	156392	10468	1028	0.501	0.769	0.849	0.1769	0.0706	0.0412	0.1198	0.0482	0.0242	51.83	88.01	97.57
<i>Southeast Asia</i>	<i>AERONET</i>	4134	504	74	0.405	0.542	0.488	0.2037	0.1447	0.1198	0.1274	0.0988	0.0821	50.17	56.15	60.81
	<i>TERRA</i>	402465	27058	2500	0.470	0.753	0.872	0.1730	0.0729	0.0342	0.109	0.0455	0.0198	57.25	87.01	97.96
<i>Eastern China</i>	<i>AERONET</i>	7396	927	118	0.513	0.551	0.356	0.3571	0.2355	0.1933	0.2038	0.1392	0.1382	40.10	49.84	50.00
	<i>TERRA</i>	241185	17324	1518	0.523	0.811	0.895	0.1646	0.0638	0.0302	0.1073	0.0435	0.0225	55.77	88.07	98.88
<i>Northeast Asia</i>	<i>AERONET</i>	9979	1178	142	0.569	0.593	0.367	0.4941	0.3249	0.2604	0.2924	0.2425	0.2202	35.17	29.54	21.13
	<i>TERRA</i>	78823	5485	467	0.553	0.872	0.965	0.1973	0.0636	0.0263	0.1201	0.0440	0.0198	56.48	87.77	98.29

<i>India</i>	<i>AERONET</i>	<u>2208</u>	<u>203</u>	<u>32</u>	<u>0.521</u>	<u>0.462</u>	<u>0.534</u>	<u>0.2957</u>	<u>0.3015</u>	<u>0.3588</u>	<u>0.2049</u>	<u>0.2283</u>	<u>0.2862</u>	<u>32.11</u>	<u>24.63</u>	<u>15.63</u>
	<i>TERRA</i>	<u>179928</u>	<u>9564</u>	<u>862</u>	<u>0.526</u>	<u>0.815</u>	<u>0.915</u>	<u>0.1564</u>	<u>0.0599</u>	<u>0.0352</u>	<u>0.1089</u>	<u>0.042</u>	<u>0.0238</u>	<u>55.16</u>	<u>90.43</u>	<u>98.14</u>

662 less than 0.01, the RMSE of 85% is less than 0.15, and the percentage falling within the EE of 67%
 663 is greater than 60%. More than 85% of stations fall within the EE is greater than 60% in Europe,
 664 North America, and Oceania, while 40-60% in South America, Africa, and Asia. The percentage of
 665 expected error is low in South and East Asia, and Central Africa, with some underestimation. Above
 666 60% in Africa, Asia, North America, and Europe have a correlation coefficient greater than 0.4. The
 667 regions with lower correlation are the coastal regions of South America, eastern Africa, western
 668 Australia, northeastern North America, and northern Europe. Above 90% of the RMSE in Europe,
 669 North America, and Oceania have a correlation coefficient smaller than 0.15. High RMSE regions
 670 are in western North America, Asia, central South America, and central Africa.
 671 Compared to AERONT daily AOD, the R of 74% stations is greater than 0.4, and the spatial
 672 distribution is similar to Terra's. The mean bias of 44% is less than 0.01, the RMSE of 68% is less
 673 than 0.15, and the percentage falling within the EE of 53% is greater than 60%. More than 70% of
 674 sites have a correlation coefficient greater than 0.4 in Africa, Asia, Europe, and North America.
 675 More than 57% of sites have an expected error percentage of over 60% in Europe, North America,
 676 and Oceania. Except for Asia. Over 72% of sites have a RMSE less than 0.15. Except for Oceania
 677 and South America, over 71% of sites in other regions have MAE less than 0.01. Almost all sites in
 678 Asia show a negative bias, significantly underestimating. However, there is a significant
 679 overestimation in western North America and western Australia. Most sites in Asia falling within
 680 the expected error are less than 50%. High RMSE region are in Asia, India, and central Africa.
 681 The validation and comparison on the site scale show a limitation similar to the MODIS DT
 682 algorithm. In areas with high vegetation coverage, the AOD from visibility are better than those in
 683 bright areas such as deserts.



684

685 **Figure 7** Validation of VIS_AOD against Terra and AERONET AODs at each site: (a–b) correlation
686 (R), (c-d) mean bias (MB), (e-f) root mean square error (RMSE), (g-h) percentage (%) of VIS_AOD
687 within the expected error envelopes.

688 **3.3.4 Discussion and uncertainty analysis**

689 The atmospheric visibility is a horizontal physical quantity, while AOD is a column-integrated
690 physical quantity. We have linked the two variables together using machine learning methods, which
691 partially compensates for the scarcity of AOD data. However, we have to face some limitations.
692 Although the boundary layer height is considered, it is not sufficient. Pollutants such as smoke from
693 biomass burning, dust, volcanic ash, and gas-aerosol conversion of sulfur dioxide to sulfate aerosols
694 in the upper and lower troposphere can undergo long-range aerosol transport under the influence of
695 circulation. The pollution transport and aerosol conversion processes above the boundary layer are
696 still significant and cannot be ignored (Eck et al., 2023). Compared to surface visibility, bias occurs
697 when the aerosol layer rises and affects AERONET measurements and MODIS retrievals. Therefore,
698 it should be considered when using this data. If there were sufficient historical vertical aerosol
699 measurements with high temporal and spatial resolution, the results of this data would be greatly
700 improved. Although some studies use aerosol profiles from pollution transport models or assumed
701 profiles as substitutes for observed profiles (Li et al., 2020; Zhang et al., 2020), the biases introduced
702 by these non-observed profiles are still significant.

703 In machine learning, we used MODIS Aqua AOD as the target value for the model because the
704 validation results for MODIS C6.1 products have a correlation coefficient of 0.9 or higher with
705 AERONET AOD at the daily scale (Wei et al., 2019a; Wei et al., 2020). Compared to AERONET,
706 MODIS AOD provides more sample data with a high global coverage. However, apart from
707 modeling errors, the systematic biases and uncertainties of MODIS Aqua AOD cannot be ignored
708 (Levy et al., 2013; Levy et al., 2018; Wei et al., 2019a). Averaging over time scale significantly
709 reduces systematic errors but cannot diminish errors caused by emission sources and terrain.
710 Therefore, the strong correlation at monthly and annual scales indicates a substantial reduction in
711 errors (Schutgens et al., 2017). This is also one of the reasons why this dataset shows stronger
712 correlation with Terra AOD and weaker correlation with AERONET in validation.

713 The spatial matching between meteorological stations and AERONET sites may cause some biases.
714 AERONET sites are usually not co-located with meteorological stations in terms of elevation and
715 horizontal distance, this is another reason for the weak correlation between VIS_AOD and
716 AERONET AOD. The meteorological stations are located at the airport. Different horizontal
717 distances may result in meteorological stations and AERONET sites being located on different
718 surfaces (such as urban, forest, mountainous). Differences in site elevation significantly impact the
719 relationship between AOD and measured visibility. When the AERONET site is at a higher elevation
720 than the meteorological station, there may be fewer measurements of aerosols over the sea at the
721 AERONET site.

722 Different pollution levels and station elevation affect the AOD derived from visibility. The elevation
723 difference and distance between meteorological stations and AERONET sites also have an impact
724 on the validation results. Therefore, the error and performance of different AERONET AOD values,
725 station elevation, and distance were analyzed.

726 **3.3.4.1 Uncertainty with pollution level**

727 As the AOD increases, the variability of bias also increases in Figure 8 (a). Almost all mean bias
728 values are within the envelope of EE, except for 1.1-1.2 and 1.5-1.6. The average bias is 0.015
729 (AOD <0.1), with 83% of data within the EE envelopes. The mean bias is -0.0011 (AOD,0.1-0.2),
730 with 54% within the EE envelopes. The mean bias is negative (AOD, 0.3-1.0), with 20%-40%
731 falling within the EE envelopes. There is a positive bias (AOD, 1.1, 1.4 and >1.6), and there is a
732 negative bias at 1.2-1.3 and 1.5-1.6. The results indicate that as pollution level increases, the
733 negative mean bias becomes significant and the underestimation increases.

734 **3.3.4.2 Uncertainty with elevation of AERONET site**

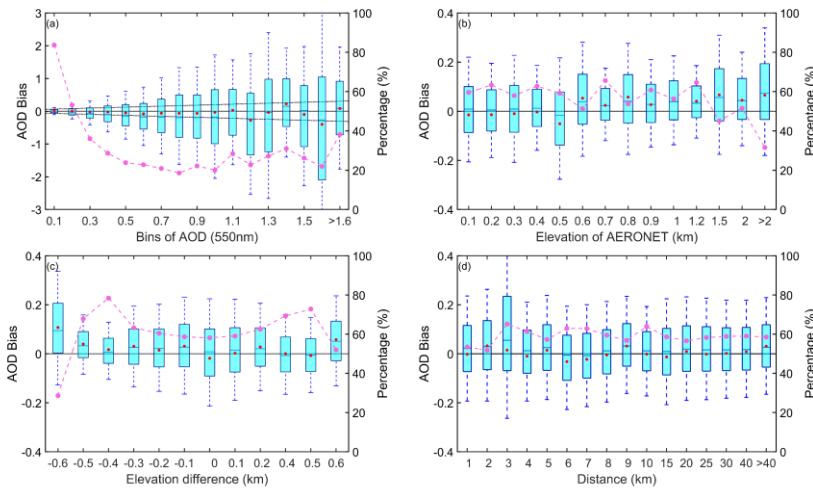
735 The contribution of particulate matter near the ground to the column aerosol loading is significant.
736 The elevation of the site affects the measurement of column aerosol loading in Figure 8 (b). There
737 is a negative bias in the low elevation (<=0.5km) with a percentage of 60%-64% falling within the
738 EE envelopes and a positive bias in high elevation (0.5-1.2km) with a percentage of 50%-65%
739 falling within the EE envelopes. The percentage significantly decreases (>1.2km), and the average
740 bias increases. Therefore, the elevation of AERONET's site will cause bias in validation, and, the
741 uncertainty greatly increases in high elevation.

742 **3.3.4.3 Uncertainty with elevation of meteorological station**

743 Due to the elevation difference between the meteorological station and AERONET site in the
744 vertical direction, the uncertainty caused by elevation differences of site was analyzed in Figure 8
745 (c). When the elevation difference is negative (the elevation of the meteorological station is lower
746 than that of the AERONET station), there is a significant positive bias. When the difference is
747 positive, the mean bias approaches 0 or is positive. The percentage is greater than 60% (-0.5 km-
748 0.5km). The positive mean bias is greater than the negative mean bias, and the uncertainty greatly
749 increases when the elevation of meteorological stations is lower than that of AERONET sites. It
750 indicates that the contribution of the near surface aerosol to the column aerosol loading is significant
751 and cannot be ignored.

752 **3.3.4.4 Uncertainty with distance between meteorological station and AERONET site**

753 The spatial variability of aerosols is significant. Meteorological stations and AERONET sites are
754 not collocated, resulting in a certain distance in spatial matching. In this study, the upper limit of
755 distance is 0.5 degree. Figure 8 (d) shows the error of the distance between stations, where the
756 degree is converted to the distance at WGS84 coordinates. The bias does not change significantly
757 with increasing distance. The average bias is around 0, with the maximum positive mean bias
758 (0.0322) at a distance of 2km and the maximum negative mean deviation (-0.0323) at 6km. The
759 median is almost positive, except at 5km and 6km. The percentage falling within the EE envelopes
760 is over 50%, with the maximum percentage (66%) at 3km and the minimum (62%) at 2km.



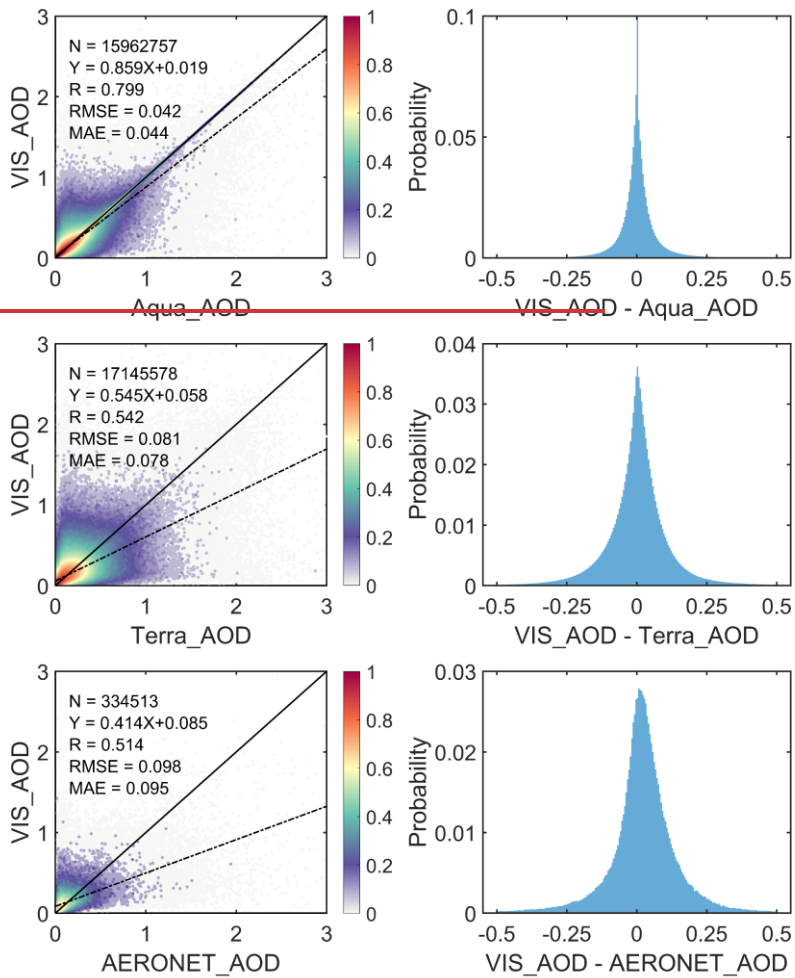
761

762 **Figure 8** Box plots of AOD bias and the percentage falling within the EE envelopes (curves): (a)
 763 AERONET AOD levels, (b) elevation of AERONET sites, (c) elevation difference between
 764 meteorological stations and AERONET sites, (d) distance (km) between meteorological stations and
 765 AERONET sites. The black horizontal line represents the zero bias. For each box, the upper, lower,
 766 and middle horizontal lines, and whiskers represent the AOD bias 75th and 25th percentiles, median,
 767 and 1.5 times the interquartile difference, respectively. The black solid lines represent the EE
 768 envelopes $(\pm(0.05+0.15*AOD_{AERONET}))$. No site with a difference of $+0.3km$ (x-axis label without
 769 0.3) in (c).

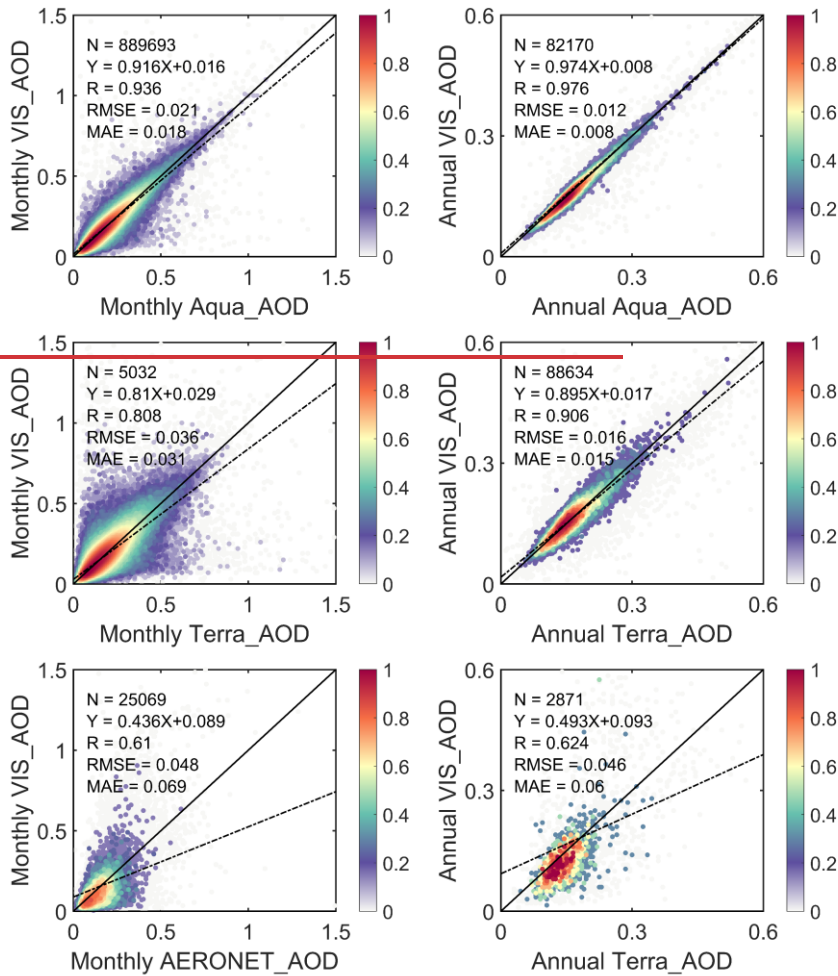
770 Figure 6 shows the scatter density plots and probability distribution of the bias between daily VIS_AOD
 771 and Aqua AOD, Terra AOD, and AERONET AOD. The R of 15,962,757 pairs data between VIS_AOD
 772 and Aqua AOD is 0.799, higher than the R between AERONET AOD and Aqua AOD, as well as Terra
 773 AOD and Aqua AOD. The RMSE is 0.042 and the MAE is 0.044. Then, 69.7% of the data pairs have a
 774 bias within ± 0.044 , and 69.7% have a bias within ± 0.093 . The R of 17,145,578 pairs of data between
 775 VIS_AOD and Terra AOD is 0.542, the RMSE is 0.081 and the MAE is 0.078. Then, 66.8% of the data
 776 pairs have a bias within ± 0.078 , and 73.3% have a bias within ± 0.095 . The R of 334,513 data pairs
 777 between VIS_AOD and AERONET AOD is 0.514. The RMSE is 0.098 and the MAE is 0.095. Finally,
 778 78.3% of the data pairs have a bias within ± 0.095 .

779 At the monthly and annual scales, RMSE and MAE show a significant decrease between VIS_AOD and
 780 Aqua, Terra, and AERONET AOD, and R shows a significant increase in Figure 7. The monthly RMSEs
 781 are 0.021, 0.036, and 0.048, the monthly MAEs are 0.018, 0.031, and 0.069, and the R values are 0.936,
 782 0.808, and 0.61, respectively. The RMSE values at the annual scale are 0.012, 0.016, and 0.025, the MAE
 783 values are 0.008, 0.015, and 0.006, and the R values are 0.976, 0.0906, and 0.624, respectively. The
 784 monthly and annual R is slightly higher than those in previous studies (Wang et al., 2009; Wu et al., 2014;
 785 Zhang et al., 2017). In addition to the differences between models, it may also be related to the calculation
 786 method of daily average visibility and the consideration of boundary layer height.

787 Overall, the results highlighted above demonstrate a clear improvement in performance on the monthly
 788 and annual scales compared to the daily scale. However, the AERONET AOD results are slightly inferior
 789 to those of Aqua and Terra AOD, which could be caused by the representativeness of the AERONET
 790 station spatial coverage and measurement error (Holben et al., 1998). Nevertheless, the results indicate
 791 the high reliability and strong predicted capability of the model, and the visibility-derived AOD can be
 792 used for aerosol climatology.



793
 794 **Figure 6** Scatter density plots and bias probability between predicted AOD (VIS_AOD) and Aqua
 795 MODIS AOD, Terra MODIS AOD and AERONET ground based observations of AOD at the daily
 796 scale. The solid black line represents the 1:1 line and the dashed black line is the linear regression
 797 line.



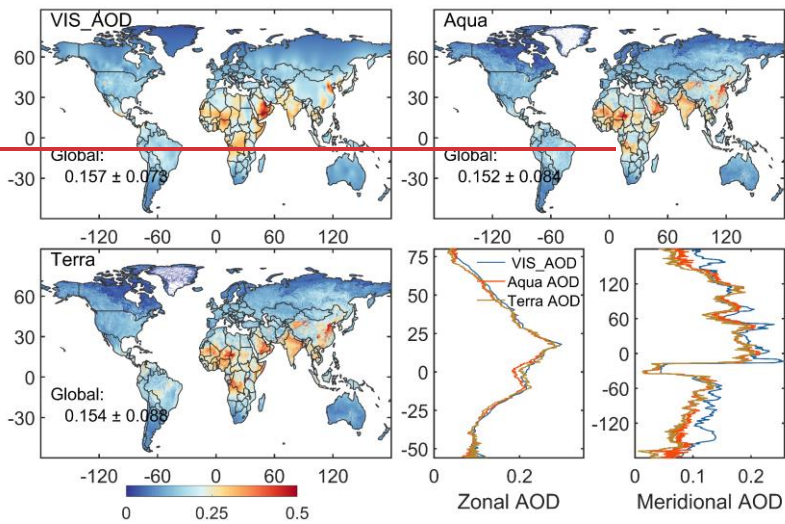
798

799 **Figure 7** Scatter density plots and bias probability between VIS_AOD and Aqua MODIS AOD,
 800 Terra MODIS AOD and AERONET ground-based observations of AOD at the monthly and annual
 801 scales. The solid black line represents the 1:1 line and the dashed black line is the linear regression
 802 line.

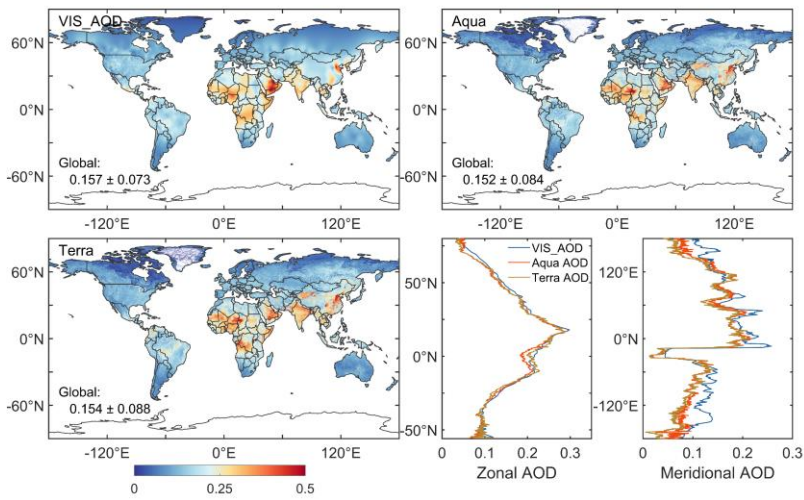
803 **3.4 Evaluation of gGridded visibility-derived AOD**

804 Figure 8-9 shows the gridded AOD based on ordinary kriging interpolation with the area-weighted
 805 method and compares the multi-year spatial, zonal, and meridional distributions of AOD with Aqua
 806 and Terra AOD over land from 2003 to 2021. The VIS_AOD is 0.157 ± 0.073 over land, which is
 807 almost equal to the Aqua (0.152 ± 0.084) and Terra (0.154 ± 0.088) AOD values with relative biases
 808 of 3.3%, and 1.9%, respectively. In order to compare the spatial correlation, Aqua and Terra MODIS
 809 AOD are averaged to the 0.5-degree resolution. In the heatmap (Figure 9 Figure 10), the R of

810 VIS_AOD and Aqua AOD is 0.7988, the RMSE is 0.049 with a bias of 32% compared to the mean,
811 and the MAE is 0.008, with a bias of 5% compared to the mean. Compared to Terra AOD, the R is
812 0.7879, and the RMSE is 0.051, with a bias of 33% compared to the mean, and the MAE is 0.005,
813 with a bias of 3% compared to the mean. ~~The R between Aqua and Terra AOD are highly similar,~~
814 ~~with an R of 0.980. By comparing the zonal and meridional distributions of AOD, VIS_AOD is~~
815 ~~consistent with Aqua and Terra AOD, with~~ ~~The R values between VIS_AOD and Aqua and Terra~~
816 ~~AOD are of 0.9957 and 0.9909 for the zonal distribution and 0.986 and 0.8979 for the meridional~~
817 distribution, respectively. In the low aerosol loading region, VIS_AOD exhibits a little
818 overestimation. Whether in meridional or zonal distribution, the peak and valley regions are
819 basically consistent (Tian et al., 2023). Due to the limitations of satellite inversion algorithms, a bias
820 appears on the bright surface, especially in northern North America with extensive snow cover
821 (Levy et al., 2013). All above results suggest that the gridded AOD is highly consistent with satellite
822 observations in spatial distribution.

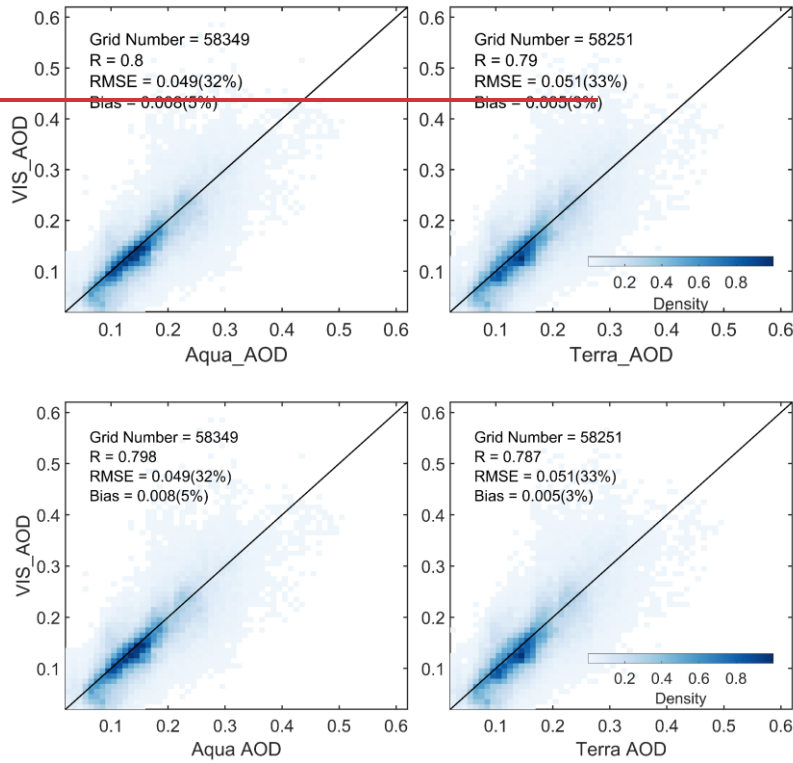


823



824

825 **Figure 8-2** The spatial, zonal and meridional distributions of the multi-year mean VIS_AOD, Aqua
 826 AOD, and Terra AOD over land from 2003 to 2021.



827

828

829 **Figure 109** Heatmap of multi-year mean gridded VIS_AOD and Aqua AOD and Terra AOD during
830 2003-2021. Terra and Aqua AOD are averaged onto a grid of 0.5°.

831 **3.5 Interannual variability and trend of visibility-derived AOD over global land**
832 **Global spatiotemporal variation of AOD in 1980-2021**

833 The evaluation of visibility-derived AOD has demonstrated that the numerical and spatial
834 distributions of VIS_AOD are in good agreement with the observations. Therefore, we employed
835 VIS_AOD to analyze the spatiotemporal and seasonal distributions, and trends over land from 1980
836 to 2021. The analytical findings are shown as follows. The AOD mentioned below is the AOD
837 derived from visibility.

838 We first analyzed the spatial distribution of multi-year average AOD from 1980 to 2021 over land
839 is shown in Figure 11 (a), from 1980 to 2021 and separately for the Southern Hemispheres (SH, -60-
840 0°N) and Northern Hemisphere (NH, 0-85°N) in Figure 10 (a). The mean AOD of land (-60-85°N),
841 NH and Northern Hemisphere (NH, 0-85°N), and the Southern Hemispheres (SH, -60-0°N) SH is
842 0.161 ± 0.074 , 0.158 ± 0.076 , and 0.173 ± 0.059 , respectively. The AOD values of Africa, Asia,
843 Europe, North America, Oceania, and South America are 0.241, 0.222, 0.110, 0.111, 0.129 and 0.117,
844 respectively.

845 Due to the influence of geography, atmospheric circulation, population, and emissions, the AOD

846 varies in different latitudes. Figure 12 illustrates the multi-year average AOD in different latitude
847 ranges for land, the NH, and the SH from 1980 to 2021. Within [-20, 20°N], the global average AOD
848 reaches its maximum (0.234), and the maximum AOD NH is 0.256 in [0, 20°N]. The highest AOD
849 in SH is 0.217 in in [-15, 0°N]. The average AOD in SH rapidly decreases from -15°N to -35°N. In
850 NH, AOD is generally greater than in SH from 5°N to 65°N. When, the latitude is greater than 70°N,
851 the NH's AOD is smaller than the SH's.

852 There are many regions of High AOD values occur in the NH, and align with the distribution of
853 population density. Approximately 7/8 of the global population resides in the NH, with 50%
854 concentrated at 20°N-40°N (Kummu et al., 2016), indicating a significant impact of human activities
855 on aerosols. The highest AOD values are observed near 17°N, including the Sahara Desert, Arabian
856 Peninsula, and southeastern India, suggesting that in addition to anthropogenic sources, deserts also
857 play a crucial role in aerosol emissions. Lower AOD regions of the SH are from 25°S to 60°S values
858 are found in the 25°S region of the SH, encompassing Australia, southern Africa, and southern South
859 America, indicating lower aerosol burdens in these areas. Additionally, North America also exhibits
860 low aerosol loading. Chin et al. (2014) analyzed the AOD over land from 1980 to 2009 with the
861 Goddard Chemistry Aerosol Radiation and Transport model, which is similar to the visibility-
862 derived AOD. The spatial distribution is consistent with the satellite results (Remer et al., 2008; Hsu
863 et al., 2012; Hsu et al., 2017; Tian et al., 2023). The AOD and extinction coefficient retrieved from
864 visibility show a similar distribution at global scale, with a correlation coefficient of nearly 0.6
865 (Mahowald et al., 2007). Similar global (Husar et al., 2000; Wang et al., 2009) and regional
866 (Koelemeijer et al., 2006; Wu et al., 2014; Boers et al., 2015; Zhang et al., 2017; Zhang et al., 2020)
867 spatial distributions have been reported.

868 AOD loadings exhibit significant seasonal variations worldwide, particularly over land. In this study,
869 a year is divided into four parts: December-January-February (DJF), March-April-May (MAM),
870 June-July-August (JJA), and September-October-November (SON), corresponding to winter
871 (summer), spring (autumn), summer (winter), and autumn (spring) in NH (SH), respectively. Figure
872 11 Figure 10 (b-e) also depicts the spatial distribution of seasonal average AOD over land from 1980
873 to 2021. The global AOD in DJF, MAM, JJA, and SON is 0.158 ± 0.062 , 0.162 ± 0.081 , 0.175 ± 0.093 ,
874 and 0.153 ± 0.070 , respectively. The standard bias of AOD in JJA and MAM are greater than those
875 in DJF and SON. AOD exhibits seasonal changes, with the highest in JJA, followed by MAM, DJF,
876 and SON. From 1980 to 2021, the seasonal AOD in NH is 0.152 ± 0.064 (DJF), 0.161 ± 0.088 (MAM),
877 0.176 ± 0.090 (JJA), and 0.144 ± 0.060 (SON), and in SH is 0.184 ± 0.041 (DJF), 0.166 ± 0.044 (MAM),
878 0.169 ± 0.072 (JJA), and 0.19 ± 0.060 (SON).

879 In NH, the AOD ranking from high to low in season is summer > spring > winter > autumn. In SH,
880 the AOD ranking from high to low in season is spring > summer > winter > autumn. The highest
881 AOD is observed during JJA in NH, while in SH, the peak occurs during SON. The occurrence of
882 high AOD values is highly associated with the growth of hygroscopic particle and the photochemical
883 reaction of aerosol precursors under higher relative humidity, the intensification of industrial
884 activities in Asia (JJA) (Remer et al., 2008) and Europe such as Russia (JJA), and biomass burning
885 in South America (SON), Southern Africa (SON), and biomass burning in Indonesia (SON)
886 (Ivanova et al., 2010; Krylov et al., 2014), and the increased dust emissions in Middle East region
887 related to the transport of dust from the Sahara region (Remer et al., 2008; Prakash et al., 2014). On
888 the other hand, the lowest global AOD values are observed during autumn, which may be attributed

889 to the ~~weakening of influence of~~ monsoon systems (Li et al., 2016; Zhao et al., 2019).

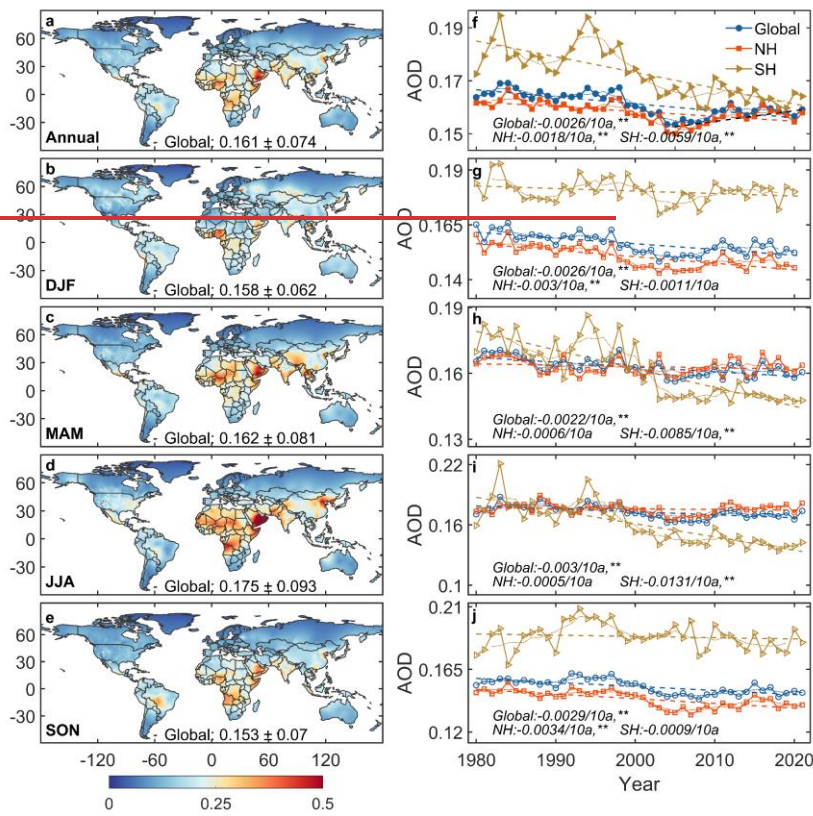
890 In addition to the spatial characteristics of AOD, the temporal variations in AOD have also been of
891 great interest due to the significant relationship between aerosols and climate change. ~~Figure~~
892 ~~10~~Figure 11 (f) shows the temporal trends of annual average AOD (** represents passing the
893 significance test, $p < 0.01$) over the global land, the SH and the NH during 1980-2021. The global
894 land, NH, and SH trends demonstrate decreasing trends of AOD with values of $-0.0026/10a$, $-$
895 $0.0018/10a$, and $-0.0059/10a$, respectively, with all passing the significance test with a confidence
896 level of 95%. Notably, the declining trend is much greater in the SH than in the NH. ~~It may be~~
897 ~~related to the decrease in the frequency of sandstorms and wildfires and the increase in precipitation,~~
898 ~~such as in Australia. The MODIS satellite results (including oceans) indicate trends of $0.004/10a$,~~
899 ~~$0.009/10a$, and $-0.002/10a$ for the global, SH, and NH, respectively, during the period of 2003-2020.~~
900 ~~This findings suggest a growth trend in the global and NH and a declining trend in SH (Tian et al.,~~
901 ~~2023). The trend of SeaWiFS AOD was $0.0058/10a$ over land during 1998-2010 (Hsu et al., 2012).~~
902 ~~Our study has the same downward signal as that in previous studies.~~ Two AOD peaks in 1983 and
903 1994 and two AOD valleys in 1980 and 1990 are observed before 2000. The two AOD peaks may
904 be attributed to large volcanic eruptions, which has been confirmed by previous studies. The
905 volcanic eruptions and their associated fires of the El Chichón volcano in Mexico in 1982 (Hirono
906 and Shibata, 1983) and Mount Pinatubo in the Philippines in 1991 (Tupper et al., 2005) resulted in
907 elevating global AOD levels in the following years. The AOD recovery to the previous low levels
908 after volcanic eruptions takes approximately 10 years (Chazette et al., 1995; Sun et al., 2019). This
909 further indicates the efficiency of our data capturing the volcanic eruption emission features. ~~also~~
910 ~~indicates that our data effectively captures this feature.~~

911 ~~Due to the influence of geography, atmospheric circulation, population, and emissions, the trend of~~
912 ~~global aerosols varies in different latitude Figure 12 illustrates the multi-year average AOD in~~
913 ~~different latitude ranges for land, the NH, and the SH from 1980 to 2021. Within $[-20, 20^{\circ}N]$, the~~
914 ~~global average AOD reaches its maximum (0.234), and the maximum AOD NH is 0.256 in $[0, 20^{\circ}N]$.~~
915 ~~The highest AOD in SH is 0.217 in $[-15, 0^{\circ}N]$. The average AOD in SH rapidly decreases from $-$~~
916 ~~$15^{\circ}N$ to $-35^{\circ}N$. In NH, AOD is generally greater than in SH from $5^{\circ}N$ to $65^{\circ}N$. When, the latitude~~
917 ~~is greater than $70^{\circ}N$, the NH's AOD is smaller than the SH's, which may be related to low emission~~
918 ~~intensity and low population density in high latitude areas.~~

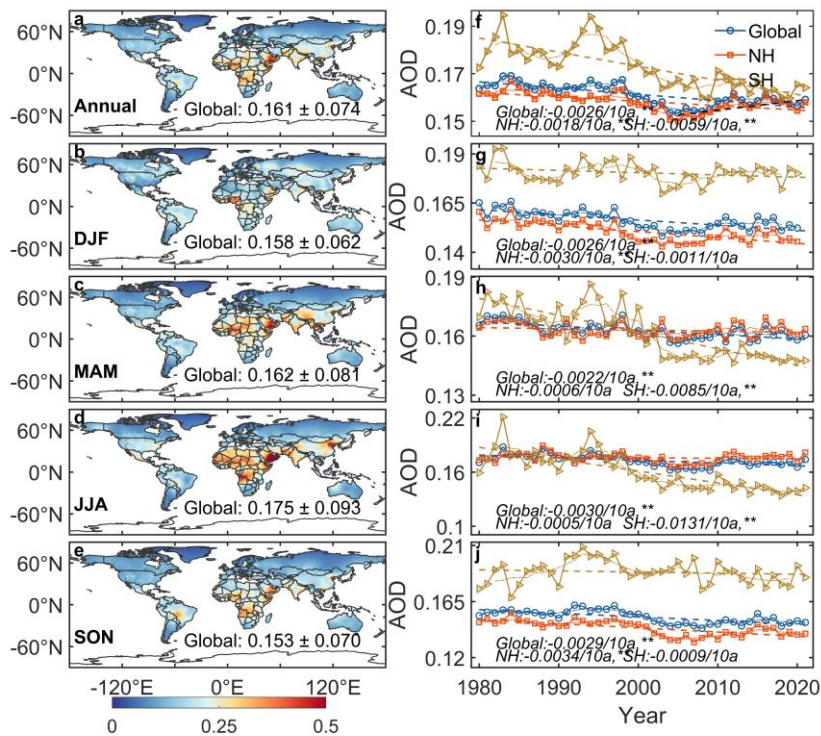
919 The ~~distinct~~ seasonal trends of AOD during 1980-2021 at the global and hemispheric scales are
920 shown in ~~Figure 10~~Figure 11 (g-j). The global AOD shows a decreasing trend in all seasons ($-$
921 0.002 ~ $-0.003/10a$). The large declining trends are observed in JJA and SON, with decreasing trend
922 values of $-0.003/10a$ and $-0.0029/10a$, respectively. DJF and MAM follow with decreasing trend
923 values of $-0.0026/10a$ and $-0.0022/10a$, respectively, all passing the significance test ($p < 0.01$). For
924 the NH, the AOD trends in different seasons are $-0.0030/10a$ (DJF), $-0.0006/10a$ (MAM), $-$
925 $0.0005/10a$ (JJA), and $-0.0034/10a$ (SON). DJF and SON pass the significance test ($p < 0.01$), while
926 MAM and JJA do not. In the SH, the trends are as follows: $-0.0011/10a$ (DJF), $-0.0085/10a$ (MAM),
927 $-0.0131/10a$ (JJA), and $-0.0009/10a$ (SON). Interestingly, in contrast to the NH, MAM and JJA pass
928 the significance test, while DJF and SON do not. The largest declining season in the NH is winter,
929 while in the SH, it is summer. The decreasing trend in the SH is more than four times greater than
930 that in the NH, particularly before the year 2000. While both the global and SH AOD exhibit a
931 decreasing trend since 2005, the NH has shown a significant increase in winter AOD, leading to an

932 overall increasing trend. Moreover, the NH shows an increasing trend of 0.004/10a from 2005 to
 933 2021.

934 Annual SO₂ emissions increased from 9.4 to 15.3 TgS from 2000 to 2005, which ultimately ended
 935 up as sulfate aerosols, leading to a significant increase in sulfate aerosols (Hofmann et al., 2009).
 936 More relevantly, the frequent volcanic eruptions in tropical regions from 2002 to 2006, combined
 937 with seasonal circulation patterns during winter, led to the transport of aerosol particles to higher
 938 latitudes (Hofmann et al., 2009; Vernier et al., 2011; Sawamura et al., 2012; Andersson et al., 2015).

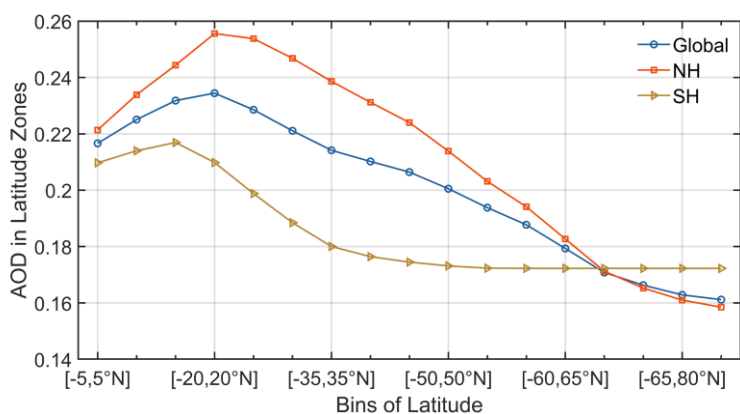


939



940

941 **Figure 10-11** The multi-year averages of VIS_AOD from 1980 to 2021. Global land (circle),
 942 northern hemisphere (NH,0-85°N) (triangle) and southern hemisphere (SH,0-60°S) (square) annual
 943 and seasonal AOD. The symbol, **, represents that the test passed at a significance level of 0.01.
 944 DJF represents December and next January and February. MAM represents March, April, and May.
 945 JJA represents June, July, and August. SON represents September, October, and November.—



946

947 **Figure 12** The global land (blue), northern hemisphere's (red) and southern hemisphere's (yellow)*

设置了格式: 字体: 非加粗

带格式的: 题注, 段落间距段前: 0.5 行, 段后: 7.8 磅

948 multi-year average VIS AOD from 1980 to 2021 in different latitude zones. The latitude range is
949 from -60 to 85°N, with a bin of 5°.

950 3.6 Interannual variability and trend of visibility-derived AOD over regionsRegional 951 spatiotemporal variation in AOD during 1980-2021

952 The distribution of AOD over global land exhibits significant spatial heterogeneity. Large variations
953 in aerosol concentrations exist among different regions, leading to a non-uniform spatial distribution
954 of AOD globally. Accurately assessing the long-term trends of aerosol loading is a key for
955 quantifying aerosol climate change, and it is crucial for evaluating the effectiveness of measures
956 implemented to improve regional air quality and reduce anthropogenic aerosol emissions.

957 To analyze the spatiotemporal characteristics and trends of AOD in different regions, we selected
958 12 representative regions that are influenced by various aerosol sources (Wang et al., 2009; Hsu et
959 al., 2012; Chin et al., 2014), such as desert, industry, anthropogenic emissions, and biomass burning
960 emissions, which nearly cover the most land and are densely populated regions (Kummu et al.,
961 2016). These representative regions are Eastern Europe, Western Europe, Western North America,
962 Eastern North America, Central South America, Western Africa, Southern Africa, Australia,
963 Southeast Asia, Northeast Asia, Eastern China, and ~~the Middle East~~India, as shown in Figure
964 1 Figure 1.

965 We use multi-year average and seasonal average AOD to evaluate aerosol loadings (Figure 11Figure
966 13), the annual average of monthly anomalies to analyze interannual trends (Figure 14Figure 12),
967 and the seasonal average to analyze seasonal trends (Figure 15Figure 13) in 12 regions from 1980
968 to 2021.

969 We can see some differences between VIS AOD and MODIS AOD. In addition to model errors,
970 the spatial matching between meteorological stations and MODIS, terrain, surface coverage, and
971 station altitude will also bring errors. When particle transport and photochemical reactions occur
972 above the boundary layer, visibility cannot capture the feature, which will also increase the
973 uncertainty. However, bias is inevitable and can only be kept as small as possible. From the trend,
974 they have similar changing characteristics, especially on monthly and yearly scales.

975 -

976 Figure 13Figure 11 shows the regions with high aerosol loadingsAOD level from 1980 to 2021
977 (multi-year average AOD > 0.2) are in West Africa, Northeast Asia, Eastern China, and ~~the Middle~~East
978 India. The AOD values in Eastern North America, Central South America, South Africa, and
979 Southeast Asia range from 0.15 to 0.2 ~~with middle aerosol loadings~~. The AOD values in Eastern
980 Europe, Western Europe, Western North America, and Australia are less than 0.15 ~~with low aerosol~~
981 loadings.

982 Europe is an industrial region with a low aerosol loading region, and the multi-year average AOD
983 in Eastern Europe (0.144 ± 0.007) is higher than that in Western Europe (0.139 ± 0.003) during 1980-
984 2021. Eastern Europe shows a greater downward trend in AOD ($-0.0041/10a$) compared to Western
985 Europe ($-0.0021/10a$). The highest AOD is observed in JJA, the dry period when solar irradiation
986 and boundary layer height increase, with Eastern Europe at 0.161 and Western Europe at 0.162,
987 which could be due to increases in secondary aerosols, biomass burning, and dust transport from

988 the Sahara (Mehta et al., 2016). However, there are seasonal variations. In Eastern Europe, the
989 seasonal AOD ranking from high to low is JJA (0.161) > DJF (0.147) > MAM (0.138) > SON
990 (0.131), while in Western Europe, it is JJA (0.162) > MAM (0.140) > SON (0.136) > DJF (0.117).
991 The differences among seasons are larger in Western Europe. AOD in Eastern Europe shows
992 declining trends in all seasons, while it does not pass the significance test in MAM. Among four
993 seasons, SON has the largest decline trend of AOD (-0.0058/10a). In Western Europe, DJF, JJA, and
994 SON exhibit declining trends of AOD that pass the significance test, while the MAM shows a
995 significant increase trend of AOD (0.0022/10a), which may be due to eruptions of the
996 Eyjafjallajökull volcano in Iceland in spring 2010 (Karbowska and Zembrzusi, 2016). Both
997 Western and Eastern Europe experienced increasing trends in AOD during the period of 1995-2005,
998 with Western Europe showing a greater increase. However, after 2000, the decline rate accelerated
999 in both regions. The downward trend in Europe is attributed to the reduction of biomass burning,
1000 anthropogenic aerosols, and aerosol precursors (such as sulfur dioxide)(Wang et al., 2009; Chin et
1001 al., 2014; Mortier et al., 2020).

1002 North America is also an industrial region with a low aerosol loading. The average AOD values for
1003 Eastern and Western North America during 1980-2021 are 0.153 ± 0.004 and 0.131 ± 0.005 ,
1004 respectively, with the Eastern region being higher than the Western region by 0.022. From 1980 to
1005 2021, both Eastern (-0.0021/10a) and Western North America (-0.0009/10a) show a downward trend;
1006 however, the decline in the Western region is not statistically significant. And the trend is -
1007 $0.0172/10a$ from 1995 to 2005 and $0.0096/10a$ from 2005 to 2021. The average AOD values in DJF,
1008 MAM, JJA, and SON in Western North America are 0.1367, 0.1286, 0.1457, and 0.114, respectively,
1009 compared to 0.137, 0.145, 0.1913, and 0.138 in Eastern North America. The lowest AOD values of
1010 12 regions during DJF and SON are observed in Western North America (Remer et al., 2008).
1011 Specifically, in the Western region, there is a consistent increasing trend during MAM (0.004/10a)
1012 from 1980 to 2021, while JJA and SON also show an increase after 2000, except for DJF (-
1013 $0.0032/10a$). In contrast, the AOD trends in the Eastern region remain unchanged during the period
1014 1980-2021, except for MAM, which shows a stable increasing trend (0.0033/10a), while DJF, JJA,
1015 and SON exhibit decreasing trends (-0.0023/10a, -0.0040/10a, -0.0053/10a, respectively). In the
1016 Western region, the annual mean AOD started to increase after 2005, while in the Eastern region,
1017 the increase was not significant. The upward trend may be due to low rainfall and increased wildfire
1018 activities (Yoon et al., 2014). The decrease in AOD in Eastern North America is related to the
1019 reduction of sulfate and organic aerosols, as well as the decrease in anthropogenic emissions caused
1020 by environmental regulations (Mehta et al., 2016).

1021 Central South America is a relatively high aerosol loading region, sourced from biomass burning,
1022 especially in SON (Remer et al., 2008; Mehta et al., 2016), with a multi-year average AOD of
1023 0.192 ± 0.017 . There is a clear downward trend (-0.0100/10a) from 1980 to 2021, which is slightly
1024 greater than the trend (-0.0090/10a) from 1998 to 2010 (Hsu et al., 2012) and AOD decreased from
1025 1980 to 2006 (Streets et al., 2009) and from 2001 to 2014 (Mehta et al., 2016). Although DJF (0.199)
1026 and SON (0.226) have higher values compared to MAM (0.180) and JJA (0.163), the large declining
1027 trends are observed in MAM (-0.0126/10a) and JJA (-0.0167/10a). It indicates that although AOD
1028 has decreased overall, the aerosol loading caused by seasonal deforestation and biomass combustion
1029 is still large (Mehta et al., 2016).

1030 Africa is also one of the regions with a high aerosol loading worldwide. In West Africa, the average
1031 AOD is 0.275 ± 0.012 during 1980-2021, and the annual AOD shows a downward trend ($-$
1032 $0.0008/10a$, $p > 0.05$). The world's largest desert (Sahara Desert) is in West Africa, with much dust
1033 aerosol discharged. AOD values in all seasons are above 0.25, with JJA (0.301) and MAM (0.300)
1034 reaching 0.3, and DJF and SON being 0.252 and 0.250, respectively. ~~In addition to the dust source,~~
1035 ~~frequent forest fires and biomass burning result in high AOD in JJA (Tian et al., 2023).~~ The AOD
1036 in DJF ($-0.0135/10a$, $p < 0.01$) and SON ($-0.0026/10a$, $p > 0.05$) exhibit decreasing trends, while JJA
1037 ($0.0088/10a$, $p < 0.01$) and MAM ($0.0037/10a$, $p > 0.05$) show an opposite trend. The multi-year
1038 average AOD in South Africa is 0.177 ± 0.020 , lower than that of West Africa. The annual mean AOD
1039 in South Africa shows a significant decrease ($-0.0096/10a$). The AOD values range from 0.12 to 0.2
1040 during 2000-2009, dominated by fine particle matter from industrial pollution from biomass and
1041 fossil fuel combustion (Hersey et al., 2015). The average AOD values in DJF, MAM, JJA, and SON
1042 are 0.189, 0.162, 0.147, and 0.210, respectively. JJA ($-0.0268/10a$, $p < 0.01$), MAM ($-0.0126/10a$,
1043 $p < 0.01$) and SON ($-0.0001/10a$, $p > 0.05$) exhibit a downward AOD trend, while DJF ($0.0006/10a$,
1044 $p > 0.05$) shows an upward trend. AERONET and simulation results also show a decreasing trend of
1045 AOD (Chin et al., 2014).

1046 Australia is a region with a low aerosol loading. The multi-year mean AOD is 0.127 ± 0.014 during
1047 1980-2021. The AOD ranges from 0.05 to 0.15 from AERONET during 2000-2021, and ~~dust and~~
1048 ~~biomass burning wildfires~~ are an important contributors to the aerosol loading (Yang et al., 2021a).
1049 There is a downward trend of AOD ($-0.0081/10a$, $p < 0.01$), which may be related to a decrease in
1050 ~~BC dust~~ and ~~biomass burning OC~~ (Yoon et al., 2016; Yang et al., 2021a). In addition, research has
1051 shown that the forest area in Australia has increased sharply since 2000 (Giglio et al., 2013),
1052 surpassing the forest fire area of the past 14 years. The seasonal average of AOD in MAM, JJA,
1053 SON, and DJF are 0.122, 0.108, 0.125, and 0.151. The AOD in JJA is the lowest among all seasons
1054 and regions. The highest AOD is in DJF with an increasing trend ($0.0056/10a$, $p < 0.01$), while the
1055 trends during MAM, JJA and SON are $-0.0096/10a$ ($p < 0.01$), $-0.0231/10a$ ($p < 0.01$) and $-0.0042/10a$
1056 ($p < 0.01$), respectively. Ground-based and satellite observations indicate that wildfires, biomass
1057 burning and sandstorms lead to high AOD in DJF and SON. The low AOD of MAM and JJA is due
1058 to a decrease in the frequency of sandstorms and wildfires and an increase in precipitation (Gras et
1059 al., 1999; Yang et al., 2021a; Yang et al., 2021b).

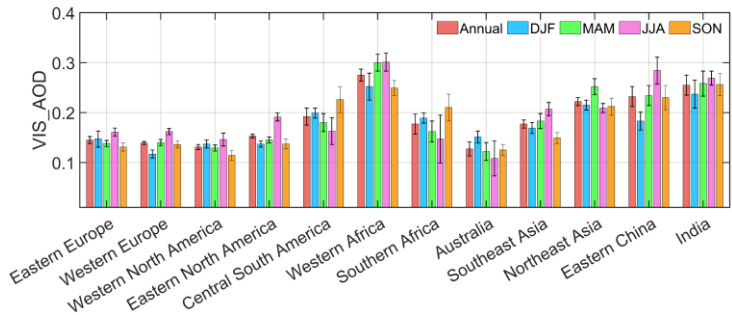
1060 Asia is also a high aerosol loading area with various sources. In Southeast Asia, the multi-year
1061 average AOD is 0.177 during 1980-2021 with a downward trend of AOD ($-0.0003/10a$, $p > 0.05$). It
1062 is also a biomass-burning area. The seasonal average AOD ranking from high to low is JJA (0.207) >
1063 MAM (0.183) > DJF (0.169) > SON (0.149). The trends in DJF ($-0.0035/10a$, $p < 0.05$), JJA ($-$
1064 $0.0007/10a$, $p > 0.05$) and SON ($-0.0021/10a$, $p > 0.05$) are opposite to MAM ($0.0050/10a$, $p < 0.01$).
1065 ~~Natural emissions were predominant in 1992 and 1997, because of the volcanic eruptions and forest~~
1066 ~~fires.~~ Southeast Asia has no clear long-term trend in estimated AOD or observed surface solar
1067 radiation (Streets et al., 2009). In Northeast Asia, the multi-year average AOD is 0.222 during 1980-
1068 2021, with no significant temporal trend. The seasonal AOD values are 0.252 in MAM, 0.215 in
1069 DJF, 0.212 in SON and 0.209 in JJA. AOD in MAM is significantly higher than other seasons, which
1070 may be related to sandstorms in East Asia, and the reason for the high AOD in winter may be related
1071 to the ~~low boundary layer height transportation~~. The trends of AOD in DJF ($-0.0025/10a$, $p > 0.05$),
1072 MAM ($0.0031/10a$, $p > 0.05$), JJA (0) and SON ($-0.0006/10a$, $p > 0.05$) are not significant. In Eastern

1073 China, the multi-year average AOD is 0.233, with an increasing trend (0.0071/10a, $p < 0.01$). The
1074 trend is 0.0151/10a from 1980 to 2006 and -0.0469/10a from 2006 to 2021. The seasonal average
1075 AOD ranking from high to low is JJA (0.284), MAM (0.234), SON (0.230) and DJF (0.183). The
1076 AOD trends in DJF (0.0093/10a, $p < 0.01$), MAM (0.0092/10a, $p < 0.01$), JJA (0.0038/10a, $p > 0.05$)
1077 and SON (0.0065/10a, $p < 0.05$) are all positive but the trend in JJA does not pass the significance
1078 test. We can see that there are three stages of changes in AOD: 1980-2005, 2006-2013 and 2014-
1079 2021. In the first stage, AOD increased steadily. In the second stage, AOD maintained a larger
1080 positive anomaly accompanied by oscillations-high level of volatility. The third stage experienced a
1081 rapid decline, reaching the level of the 1980s by 2021. The increasing trend of AOD before 2006
1082 may be due to the significant increase in industrial activity, and after 2013, the significant decrease
1083 is closely related to the implementation of air quality-related laws and regulations, along with
1084 adjustments in the energy structure (Hu et al., 2018; Cherian and Quaas, 2020).

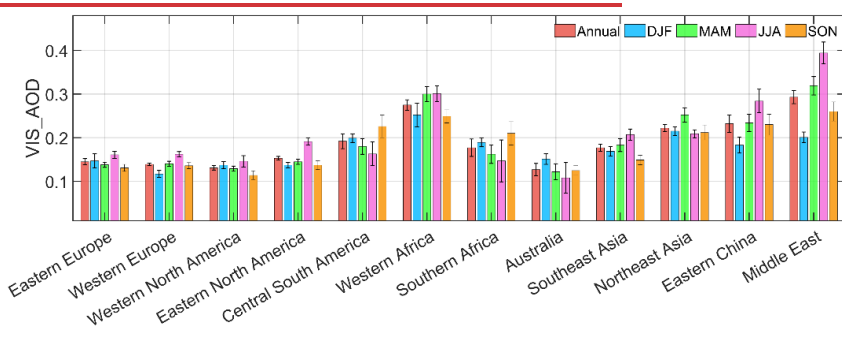
1085 India is a high aerosol loading area. The multi-year average AOD is 0.255, with an upward trend
1086 (0.0096/10a, $p < 0.01$) from 1980 to 2021. Dust and biomass burning has an influence on AOD level.
1087 There are three stages: 1980-1997 (0.0032/10a, $p < 0.01$), 1997-2005 (-0.0420/10a, $p < 0.01$), 2005-
1088 2021 (0.0481/10a, $p < 0.01$). Although the trend is downward in the second stage, the larger positive
1089 trend is in the third stage. The seasonal average AOD values are 0.237 in DJF, 0.258 in MAM, 0.269
1090 in JJA, and 0.256 in SON. The largest AOD is in JJA. In winter and autumn, it affected by biomass
1091 burning, and in spring and summer, it is also affected by dust, transported from the Sahara under
1092 during the monsoon period (Remer et al., 2008). The trends in DJF (0.0152/10a, $p < 0.01$), MAM
1093 (0.0091/10a, $p < 0.01$), JJA (0.0025/10a, $p > 0.05$), and SON (0.0107/10a, $p < 0.05$) are positive. There
1094 largest trend is in winter. In the Middle East, aerosols are influenced by local deserts and aerosols
1095 transport from Africa and petroleum-related industries, resulting in high aerosol loading (Wei et al.,
1096 2019a; Wei et al., 2019b). The multi-year average AOD is 0.293, which is the highest among all 12
1097 study regions, with an upward trend (0.0027/10a, $p > 0.05$). The aerosol loading was higher during
1098 1980-1990 and 2000-2021 and lower during 1990-2000. The seasonal average AOD values are
1099 0.201 in DJF, 0.319 in MAM, 0.394 in JJA, and 0.26 in SON. The trends of AOD in DJF (-
1100 0.0039/10a, $p < 0.05$) and SON (-0.0012/10a, $p > 0.05$) show an upward trend, while the trends in
1101 MAM (0.0067/10a, $p < 0.05$) and JJA (0.0095/10a, $p < 0.01$) are opposite. This increasing trend is
1102 related to sand and dust emissions (Klingmüller et al., 2016).

1103

1104 To summarize, there are significant differences in the spatial distribution, annual trends, and
1105 seasonal trends of AOD across different regions from 1980 to 2021. The high aerosol loadings
1106 from 1980 to 2021 are in West Africa, Middle East and Asia, and low aerosol loading regions
1107 are in Europe, Western North America, and Australia. Eastern China and Middle East show
1108 an increasing trend, Southeast Asia and Northeast Asia show no significant trend, and the other
1109 regions show downward trends. However, not all regional seasonal trends are consistent with their
1110 annual trends. The results in this study have supplemented the long-term trend and distribution of
1111 AOD over land.

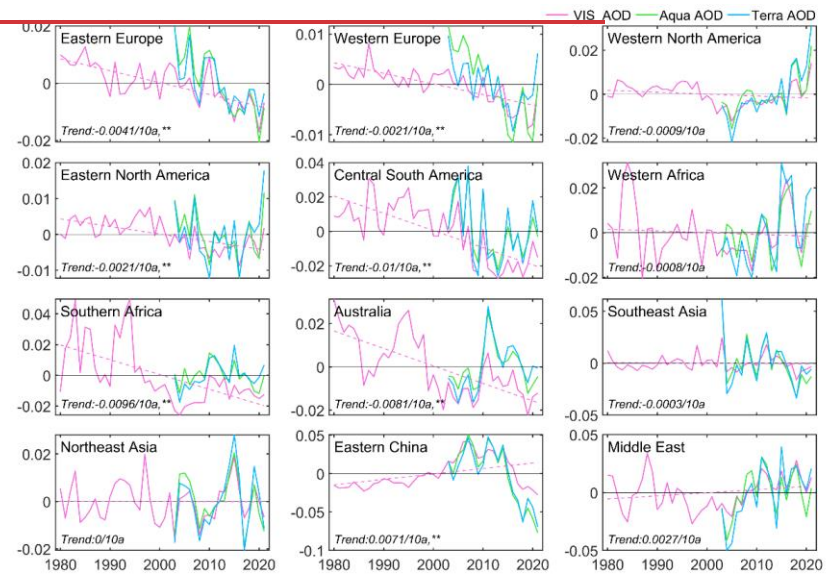


1112

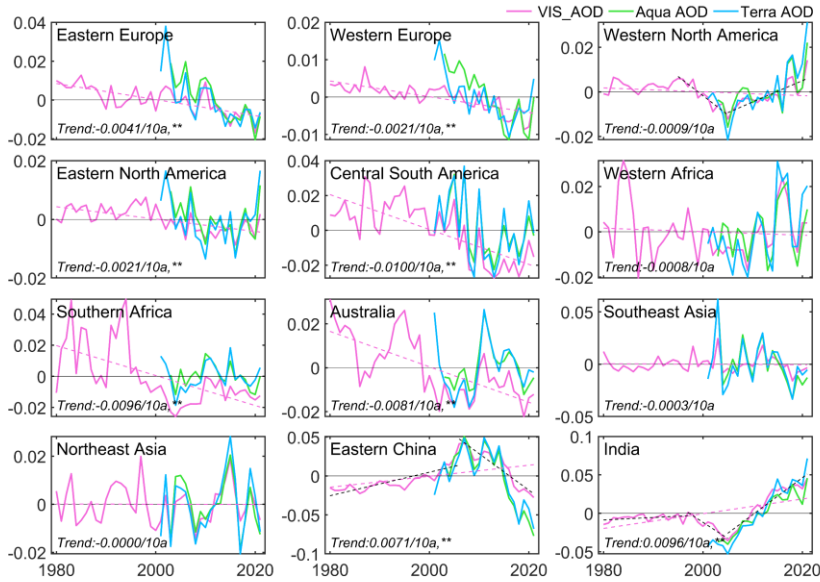


1113

1114 **Figure 13** Figure 41 Annual and seasonal averages of AOD in 12 regions during 1980-2021.

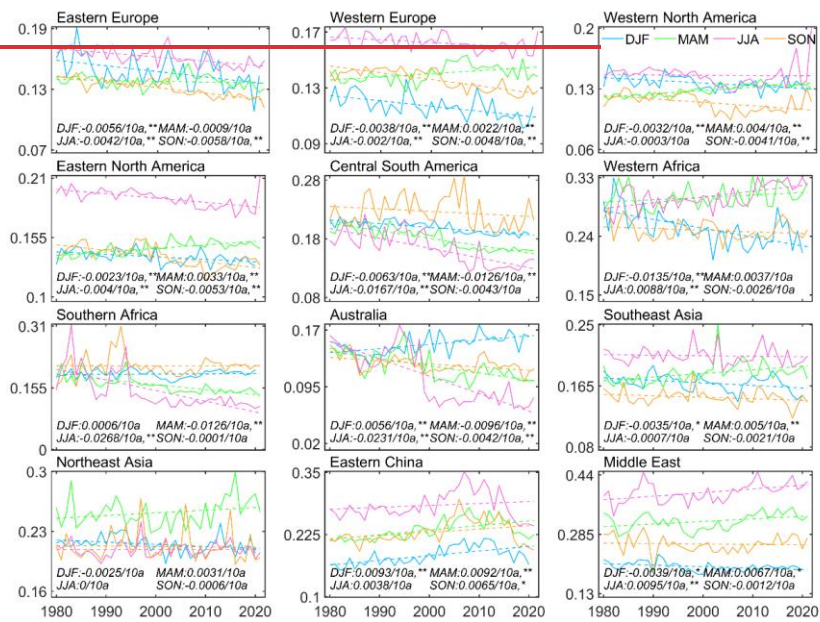


1115



1116

1117 **Figure 14** Figure 12 Annual averages of monthly anomaly gridded VIS_AOD (pink line), Aqua
 1118 (green line), and Terra (blue line) MODIS AOD in 12 regions. The dotted line is the trend line.
 1119 VIS_AOD has good temporal consistency with Aqua and Terra MODIS AOD from 2003 to 2021.



1120



带格式的: 正文, 段落间距段前: 0 磅, 段后: 0 磅
 设置了格式: 字体: (中文) + 中文正文 (等线), (无)

1121

1122 **Figure 15** Figure 13 Seasonal averages of gridded VIS AOD during 1980 to 2021 in 12 regions
 1123 (Eastern Europe, Western Europe, Western North America, Eastern North America, Central South
 1124 America, Western Africa, Southern Africa, Australia, Southeast Asia, Northeast Asia, Eastern China,
 1125 and Middle EastIndia). The dotted line is the trend line.

1126 4 Data availability

1127 The visibility-derived AOD at station and grid scales over global land from 1980 to 2021 are
 1128 available at National Tibetan Plateau / Third Pole Environment Data Center
 1129 (<https://doi.org/10.11888/Atmos.tpcdc.300822>) (Hao et al., 2023).

1130 5 Conclusions

1131 In this study, we employed a machine learning technique to derive AOD for over 5000 land stations
 1132 worldwide, based on satellite data, visibility, and related parameters. Monthly AOD was interpolated
 1133 onto a 0.5° grid using ordinary kriging with area weighting. The method was trained with Aqua
 1134 MODIS AOD. The accuracy and performance of the derived AOD were assessed and validated
 1135 against Terra MODIS AOD as well as AERONET ground-based observations of AOD for the
 1136 corresponding stations. Evaluation of the gridded AOD was conducted using Aqua and Terra
 1137 MODIS AOD. We obtained daily AOD for global land stations from 1980 to 2021, as well as
 1138 monthly gridded AOD. The two datasets complement the shortcomings of AOD in terms of time
 1139 scale and spatial coverage. Finally, the spatiotemporal variation in AOD was analyzed for global
 1140 land, the Southern Hemisphere, the Northern Hemisphere, and 12 regions in the past 42 years.
 1141 Several key findings have been obtained in this study as follows.

设置了格式: 字体: 加粗

1142 **1. Modeling and gridding evaluation performance.** The mean RMSE, MAE, and R of all stations
1143 are 0.078, 0.044, and 0.750, respectively. The RMSE of 93% stations is less than 0.11, the MAE of
1144 91% is less than 0.06, and the R of 88% is greater than 0.7, respectively.

1145 ~~2. The gridded AOD is highly consistent with the satellite observations. Compared to Aqua and~~
1146 ~~Terra, the average biases of multi-year gridded AOD compared to Aqua and Terra are 3.3% and~~
1147 ~~1.9%, and respectively. The spatial correlation coefficients are 0.80 and 0.79, with the zonal~~
1148 ~~correlation coefficients are of 0.997 and 0.99, and the meridional correlation coefficients are of~~
1149 ~~0.9986 and 0.90.~~

1150 **2. Model validation.** For the daily scale, the R, RMSE and MAE of between VIS AOD and Aqua
1151 AOD is 0.799, 0.079 and 0.044, respectively. The percentage of sample point falling within the EE
1152 envelopes is 84.12%. The R between VIS AOD and Terra AOD is 0.542, with a RMSE of 0.125
1153 and MAE of 0.078. The percentage falling within the EE envelopes is 64.76%. The R between
1154 VIS AOD and AERONET AOD is 0.546, with a RMSE of 0.186 and MAE of 0.099. The percentage
1155 falling within the EE envelopes is 57.87%. For the monthly and annual scales, RMSE and MAE
1156 show a significant decrease between VIS AOD and Aqua, Terra, and AERONET AOD, and R and
1157 percentages falling within EE show a significant increase.

设置了格式: 字体: 加粗

1158 **3. Error analysis.** The average bias is 0.015 (AOD < 0.1), with 83% of data within the EE envelopes.
1159 As pollution level increases, the negative mean bias becomes significant and the underestimation
1160 increases. There is a negative bias in the low elevation (<=0.5km) with a percentage of 60%-64%
1161 falling within the EE envelopes and a positive bias in high elevation (0.5-1.2km) with a percentage
1162 of 50%-65% falling within the EE envelopes. The elevation of AERONET's site caused a bias in
1163 high elevation. When the elevation difference is negative (the elevation of the meteorological station
1164 is lower than that of the AERONET site), there is a significant positive bias. When the difference is
1165 positive, the mean bias approaches 0 or is positive. The bias does not change significantly with
1166 increasing distance between the meteorological station and AERONET site.

1167 **4. Global land AOD.** The global, NH, and SH AOD values from 1980 to 2021 are 0.161 ± 0.074 ,
1168 0.158 ± 0.076 , and 0.173 ± 0.059 , respectively. Trends in AOD for the global, NH, and SH
1169 demonstrate a decreasing trend of $-0.0026/10a$, $-0.0018/10a$, and $-0.0059/10a$, respectively ($p < 0.01$).
1170 The seasonal AOD ranking from high to low is JJA > MAM > DJF > SON over the global land and in
1171 the NH, while in the SH, it is DJF > JJA > MAM > SON. The largest declining trends are observed in
1172 NH summer and SH winter.

1173 **4. Regional AOD.** From 1980 to 2021, regions with high aerosol loadings (AOD > 0.2) were found
1174 in West Africa, Northeast Asia, Eastern China, and ~~the Middle East~~ India. Regions with moderate
1175 aerosol loadings (AOD between 0.15 and 0.2) are Eastern North America, Central South America,
1176 South Africa, and Southeast Asia. Eastern Europe, Western Europe, Western North America, and
1177 Australia are regions with low aerosol loadings (AOD < 0.15). The trends are $-0.0041/10a$, $-$
1178 $0.0021/10a$, $-0.0009/10a$, $-0.0021/10a$, $-0.0100/10a$, $-0.0008/10a$, $-0.0096/10a$, $-0.0081/10a$, $-$
1179 $0.0003/10a$, $-0.0000/10a$, $0.0071/10a$, and $0.0096/10a$ in Eastern Europe, Western Europe, Western
1180 North America, Eastern North America, Central South America, Western Africa, Southern Africa,
1181 Australia, Southeast Asia, Northeast Asia, Eastern China, and India, respectively.

1182 **Competing interests**

1183 The contact author has declared that none of the authors has any competing interests.

1184 Acknowledgments

1185 This work was supported by the National Key Research & Development Program of China
1186 (2022YFF0801302) and the National Natural Science Foundation of China (41930970). The hourly
1187 visibility data were download from
1188 <https://mesonet.agron.iastate.edu/ASOS/>. The
1189 Aerosol Robotic Network (AERONET) ~~daily~~-15-minute aerosol optical depth (AOD) data were
1190 download from which can be downloaded from <https://aeronet.gsfc.nasa.gov>. The MODIS AOD
1191 data were download from <https://ladsweb.modaps.eosdis.nasa.gov/>.

1192

1193 References

- 1194 Ackerman, A. S., Hobbs, P. V., & Toon, O. B. (1995). A model for particle microphysics, turbulent mixing,
1195 and radiative transfer in the stratocumulus-topped marine boundary layer and comparisons with
1196 measurements. *Journal of Atmospheric Sciences*, 52(8), 1204-1236.
- 1197 Albrecht, B. A. (1989). Aerosols, cloud microphysics, and fractional cloudiness. *Science*, 245(4923),
1198 1227-1230.
- 1199 Anderson, T. L., Charlson, R. J., Bellouin, N., Boucher, O., Chin, M., Christopher, S. A., *et al.* (2005).
1200 An "A-Train" strategy for quantifying direct climate forcing by anthropogenic aerosols. *Bulletin*
1201 *of the American Meteorological Society*, 86(12), 1795-+.
- 1202 Andersson, S. M., Martinsson, B. G., Vernier, J.-P., Friberg, J., Brenninkmeijer, C. A., Hermann, M., *et*
1203 *al.* (2015). Significant radiative impact of volcanic aerosol in the lowermost stratosphere.
1204 *Nature Communications*, 6(1), 7692.
- 1205 Andrews, E., Sheridan, P. J., Ogren, J. A., Hageman, D., Jefferson, A., Wendell, J., *et al.* (2019).
1206 Overview of the NOAA/ESRL federated aerosol network. *Bulletin of the American*
1207 *Meteorological Society*, 100(1), 123-135.
- 1208 Barnaba, F., Angelini, F., Curci, G., & Gobbi, G. P. (2011). An important fingerprint of wildfires on the
1209 European aerosol load. *Atmospheric Chemistry and Physics*, 11(20), 10487-10501.
- 1210 Bergstrom, R. W., Pilewskie, P., Russell, P. B., Redemann, J., Bond, T. C., Quinn, P. K., *et al.* (2007).
1211 Spectral absorption properties of atmospheric aerosols. *Atmospheric Chemistry and Physics*,
1212 7(23), 5937-5943.
- 1213 Bescond, A., Yon, J., Girasole, T., Jouen, C., Rozé, C., & Coppalle, A. (2013). Numerical investigation
1214 of the possibility to determine the primary particle size of fractal aggregates by measuring light
1215 depolarization. *Journal of Quantitative Spectroscopy and Radiative Transfer*, 126, 130-139.
- 1216 Boers, R., van Weele, M., van Meijgaard, E., Savenije, M., Siebesma, A. P., Bosveld, F., *et al.* (2015).
1217 Observations and projections of visibility and aerosol optical thickness (1956-2100) in the
1218 Netherlands: impacts of time-varying aerosol composition and hygroscopicity. *Environmental*
1219 *Research Letters*, 10(1).
- 1220 Bokoye, A. I., Royer, A., O'Neil, N., Cliche, P., Fedosejevs, G., Teillet, P., *et al.* (2001). Characterization
1221 of atmospheric aerosols across Canada from a ground-based sunphotometer network:
1222 AEROCAN. *Atmosphere-Ocean*, 39(4), 429-456.

设置了格式: 默认段落字体, 字体: (默认) + 西文正文 (等
线), (中文) + 中文正文 (等线)

1223 Bösenberg, J., & Matthias, V. (2003). EARLINET: A European Aerosol Research Lidar Network to
1224 Establish an Aerosol Climatology. *Max Planck Institut Fur Meteorologie*.

1225 Bright, J. M., & Gueymard, C. A. (2019). Climate-specific and global validation of MODIS Aqua and
1226 Terra aerosol optical depth at 452 AERONET stations. *Solar Energy*, 183, 594-605.

1227 Browne, M. W. (2000). Cross-validation methods. *Journal of Mathematical Psychology*, 44(1), 108-132.

1228 Calvo, A. I., Alves, C., Castro, A., Pont, V., Vicente, A. M., & Fraile, R. (2013). Research on aerosol
1229 sources and chemical composition: Past, current and emerging issues. *Atmospheric Research*,
1230 120, 1-28.

1231 Chafe, Z. A., Brauer, M., Klimont, Z., Van Dingenen, R., Mehta, S., Rao, S., *et al.* (2014). Household
1232 Cooking with Solid Fuels Contributes to Ambient PM_{2.5} Air Pollution and the Burden of
1233 Disease. *Environmental Health Perspectives*, 122(12), 1314-1320.

1234 Chazette, P., David, C., Lefrère, J., Godin, S., Pelon, J., & Mégie, G. (1995). Comparative lidar study of
1235 the optical, geometrical, and dynamical properties of stratospheric post-volcanic aerosols,
1236 following the eruptions of El Chichon and Mount Pinatubo. *Journal of Geophysical Research:*
1237 *Atmospheres*, 100(D11), 23195-23207.

1238 Che, H., Xia, X., Zhu, J., Li, Z., Dubovik, O., Holben, B., *et al.* (2014). Column aerosol optical properties
1239 and aerosol radiative forcing during a serious haze-fog month over North China Plain in 2013
1240 based on ground-based sunphotometer measurements. *Atmospheric Chemistry and Physics*,
1241 14(4), 2125-2138.

1242 Che, H., Zhang, X., Chen, H., Damiri, B., Goloub, P., Li, Z., *et al.* (2009). Instrument calibration and
1243 aerosol optical depth validation of the China Aerosol Remote Sensing Network. *Journal of*
1244 *Geophysical Research-Atmospheres*, 114.

1245 Chen, A., Zhao, C., & Fan, T. (2022). Spatio-temporal distribution of aerosol direct radiative forcing over
1246 mid-latitude regions in north hemisphere estimated from satellite observations. *Atmospheric*
1247 *Research*, 266.

1248 Chen, D., Ou, T., Gong, L., Xu, C.-Y., Li, W., Ho, C.-H., *et al.* (2010). Spatial Interpolation of Daily
1249 Precipitation in China: 1951-2005. *Advances in Atmospheric Sciences*, 27(6), 1221-1232.

1250 Cherian, R., & Quaas, J. (2020). Trends in AOD, clouds, and cloud radiative effects in satellite data and
1251 CMIP5 and CMIP6 model simulations over aerosol source regions. *Geophysical Research*
1252 *Letters*, 47(9), e2020GL087132.

1253 Chin, M., Diehl, T., Tan, Q., Prospero, J., Kahn, R., Remer, L., *et al.* (2014). Multi-decadal aerosol
1254 variations from 1980 to 2009: a perspective from observations and a global model. *Atmospheric*
1255 *Chemistry and Physics*, 14(7), 3657-3690.

1256 Chu, D., Kaufman, Y., Ichoku, C., Remer, L., Tanré, D., & Holben, B. (2002). Validation of MODIS
1257 aerosol optical depth retrieval over land. *Geophysical Research Letters*, 29(12), MOD2-1-
1258 MOD2-4.

1259 Chuang, P.-J., & Huang, P.-Y. (2023). B-VAE: a new dataset balancing approach using batched
1260 Variational AutoEncoders to enhance network intrusion detection. *Journal of Supercomputing*.

1261 Deuzé, J., Goloub, P., Herman, M., Marchand, A., Perry, G., Susana, S., *et al.* (2000). Estimate of the
1262 aerosol properties over the ocean with POLDER. *Journal of Geophysical Research:*
1263 *Atmospheres*, 105(D12), 15329-15346.

1264 Dhanya, R., Paul, I. R., Akula, S. S., Sivakumar, M., & Nair, J. J. (2020). F-test feature selection in
1265 Stacking ensemble model for breast cancer prediction. *Procedia Computer Science*, 171, 1561-
1266 1570.

1267 Diner, D. J., Beckert, J. C., Reilly, T. H., Bruegge, C. J., Conel, J. E., Kahn, R. A., *et al.* (1998). Multi-
1268 angle Imaging SpectroRadiometer (MISR) instrument description and experiment overview.
1269 *IEEE Transactions on Geoscience & Remote Sensing*, 98(4), 1072-1087.

1270 Dong, Y., Li, J., Yan, X., Li, C., Jiang, Z., Xiong, C., *et al.* (2023). Retrieval of aerosol single scattering
1271 albedo using joint satellite and surface visibility measurements. *Remote Sensing of Environment*,
1272 294, 113654.

1273 Dover, J., Winans, L. J., & Ams, A. M. S. (2002). *Evaluation of windshields for use in the Automated*
1274 *Surface Observing System (ASOS)*. Paper presented at the 6th Symposium on Integrated
1275 Observing Systems, Orlando, FL.

1276 Dubovik, Oleg, Holben, Brent, Eck, Thomas, *et al.* (2002a). Variability of Absorption and Optical
1277 Properties of Key Aerosol Types Observed in Worldwide Locations. *Journal of the Atmospheric*
1278 *Sciences*, 59(3), 590-590.

1279 Dubovik, O., Holben, B., Eck, T. F., Smirnov, A., Kaufman, Y. J., King, M. D., *et al.* (2002b). Variability
1280 of absorption and optical properties of key aerosol types observed in worldwide locations.
1281 *Journal of the Atmospheric Sciences*, 59(3), 590-608.

1282 Dubovik, O., Smirnov, A., Holben, B. N., King, M. D., Kaufman, Y. J., Eck, T. F., *et al.* (2000). Accuracy
1283 assessments of aerosol optical properties retrieved from Aerosol Robotic Network (AERONET)
1284 Sun and sky radiance measurements. *Journal of Geophysical Research-Atmospheres*, 105(D8),
1285 9791-9806.

1286 Eck, T. F., Holben, B. N., Reid, J. S., Sinyuk, A., Giles, D. M., Arola, A., *et al.* (2023). The extreme forest
1287 fires in California/Oregon in 2020: Aerosol optical and physical properties and comparisons of
1288 aged versus fresh smoke. *Atmospheric Environment*, 305, 119798.

1289 Elterman, L. (1970). Relationships between vertical attenuation and surface meteorological range.
1290 *Applied Optics*, 9(8), 1804-1810.

1291 Fan, H., Zhao, C., Yang, Y., & Yang, X. (2021). Spatio-Temporal Variations of the
1292 $PM_{2.5}/PM_{10}$ Ratios and Its Application to Air Pollution Type
1293 Classification in China. *Frontiers in Environmental Science*, 9.

1294 Fernández, A., García, S., Herrera, F., & Chawla, N. V. (2018). SMOTE for learning from imbalanced
1295 data: progress and challenges, marking the 15-year anniversary. *Journal of artificial intelligence*
1296 *research*, 61, 863-905.

1297 Filonchyk, M., Yan, H., Yang, S., & Lu, X. (2018). Detection of aerosol pollution sources during
1298 sandstorms in Northwestern China using remote sensed and model simulated data. *Advances in*
1299 *Space Research*, 61(4), 1035-1046.

1300 Forster, P., Ramaswamy, V., Artaxo, P., Bernsten, T., Betts, R., Fahey, D. W., *et al.* (2007). Changes in
1301 atmospheric constituents and in radiative forcing. *Climate Change 2007: The Physical Science*
1302 *Basis. Contribution of Working Group I to the 4th Assessment Report of the Intergovernmental*
1303 *Panel on Climate Change*.

1304 Giglio, L., Randerson, J. T., & Van Der Werf, G. R. (2013). Analysis of daily, monthly, and annual burned
1305 area using the fourth-generation global fire emissions database (GFED4). *Journal of*
1306 *Geophysical Research: Biogeosciences*, 118(1), 317-328.

1307 Giles, D. M., Sinyuk, A., Sorokin, M. G., Schafer, J. S., Smirnov, A., Slutsker, I., *et al.* (2019).
1308 Advancements in the Aerosol Robotic Network (AERONET) Version 3 database – automated
1309 near-real-time quality control algorithm with improved cloud screening for Sun photometer
1310 aerosol optical depth (AOD) measurements. *Atmos. Meas. Tech.*, 12(1), 169-209.

1311 Goovaerts, P. (2000). Geostatistical approaches for incorporating elevation into the spatial interpolation
1312 of rainfall. *Journal of Hydrology*, 228(1-2), 113-129.

1313 Gras, J., Jensen, J., Okada, K., Ikegami, M., Zaizen, Y., & Makino, Y. (1999). Some optical properties of
1314 smoke aerosol in Indonesia and tropical Australia. *Geophysical Research Letters*, 26(10), 1393-
1315 1396.

1316 Guerrero-Rascado, J. L., Landulfo, E., Antuña, J. C., Barbosa, H. d. M. J., Barja, B., Bastidas, Á. E., *et*
1317 *al.* (2016). Latin American Lidar Network (LALINET) for aerosol research: Diagnosis on
1318 network instrumentation. *Journal of Atmospheric and Solar-Terrestrial Physics*, 138, 112-120.

1319 Guo, J., Zhang, J., Yang, K., Liao, H., Zhang, S., Huang, K., *et al.* (2021). Investigation of near-global
1320 daytime boundary layer height using high-resolution radiosondes: first results and comparison
1321 with ERA5, MERRA-2, JRA-55, and NCEP-2 reanalyses. *Atmospheric Chemistry and Physics*,
1322 21(22), 17079-17097.

1323 Halmer, M. M., Schmincke, H.-U., & Graf, H.-F. (2002). The annual volcanic gas input into the
1324 atmosphere, in particular into the stratosphere: a global data set for the past 100 years. *Journal*
1325 *of Volcanology and Geothermal Research*, 115(3-4), 511-528.

1326 Hao, H., Wang, K., & Wu, G. (2023). *Visibility-derived aerosol optical depth over global land (1980-*
1327 *2021)*. Retrieved from: <https://dx.doi.org/10.11888/Atmos.tpsc.300822>

1328 He, H., Bai, Y., Garcia, E. A., & Li, S. (2008). *ADASYN: Adaptive synthetic sampling approach for*
1329 *imbalanced learning*. Paper presented at the 2008 IEEE international joint conference on neural
1330 networks (IEEE world congress on computational intelligence).

1331 Herich, H., Kammermann, L., Gysel, M., Weingartner, E., Baltensperger, U., Lohmann, U., *et al.* (2008).
1332 In situ determination of atmospheric aerosol composition as a function of hygroscopic growth.
1333 *Journal of Geophysical Research: Atmospheres*, 113(D16).

1334 Hersbach, H., Bell, B., Berrisford, P., Hirahara, S., Horányi, A., Muñoz-Sabater, J., *et al.* (2020). The
1335 ERA5 global reanalysis. *Quarterly Journal of the Royal Meteorological Society*, 146(730),
1336 1999-2049.

1337 Hersey, S. P., Garland, R. M., Crosbie, E., Shingler, T., Sorooshian, A., Piketh, S., *et al.* (2015). An
1338 overview of regional and local characteristics of aerosols in South Africa using satellite, ground,
1339 and modeling data. *Atmospheric Chemistry and Physics*, 15(8), 4259-4278.

1340 Hirono, M., & Shibata, T. (1983). Enormous increase of stratospheric aerosols over Fukuoka due to
1341 volcanic eruption of El Chichon in 1982. *Geophysical Research Letters*, 10(2), 152-154.

1342 Hofmann, D., Barnes, J., O'Neill, M., Trudeau, M., & Neely, R. (2009). Increase in background
1343 stratospheric aerosol observed with lidar at Mauna Loa Observatory and Boulder, Colorado.
1344 *Geophysical Research Letters*, 36(15).

1345 Holben, B. N., Eck, T. F., Slutsker, I., Tanre, D., Buis, J. P., Setzer, A., *et al.* (1998). AERONET - A
1346 federated instrument network and data archive for aerosol characterization. *Remote Sensing of*
1347 *Environment*, 66(1), 1-16.

1348 Hsu, N., Gautam, R., Sayer, A., Bettenhausen, C., Li, C., Jeong, M., *et al.* (2012). Global and regional
1349 trends of aerosol optical depth over land and ocean using SeaWiFS measurements from 1997 to
1350 2010. *Atmospheric Chemistry and Physics*, 12(17), 8037-8053.

1351 Hsu, N., Jeong, M. J., Bettenhausen, C., Sayer, A., Hansell, R., Seftor, C., *et al.* (2013). Enhanced Deep
1352 Blue aerosol retrieval algorithm: The second generation. *Journal of Geophysical Research:*
1353 *Atmospheres*, 118(16), 9296-9315.

1354 Hsu, N., Lee, J., Sayer, A., Carletta, N., Chen, S. H., Tucker, C., *et al.* (2017). Retrieving near-global

1355 aerosol loading over land and ocean from AVHRR. *Journal of Geophysical Research:*
1356 *Atmospheres*, 122(18), 9968-9989.

1357 Hsu, N. C., Tsay, S.-C., King, M. D., & Herman, J. R. (2006). Deep blue retrievals of Asian aerosol
1358 properties during ACE-Asia. *Ieee Transactions on Geoscience and Remote Sensing*, 44(11),
1359 3180-3195.

1360 Hu, B., Zhang, X., Sun, R., & Zhu, X. (2019). Retrieval of Horizontal Visibility Using MODIS Data: A
1361 Deep Learning Approach. *Atmosphere*, 10(12).

1362 Hu, K., Kumar, K. R., Kang, N., Boiyo, R., & Wu, J. (2018). Spatiotemporal characteristics of aerosols
1363 and their trends over mainland China with the recent Collection 6 MODIS and OMI satellite
1364 datasets. *Environmental Science and Pollution Research*, 25, 6909-6927.

1365 Husar, R. B., Husar, J. D., & Martin, L. (2000). Distribution of continental surface aerosol extinction
1366 based on visual range data. *Atmospheric Environment*, 34(29-30), 5067-5078.

1367 IPCC (2021). *Climate Change 2021: The Physical Science Basis*, Cambridge University Press, New York.

1368 Ivanova, G., Ivanov, V., Kukavskaya, E., & Soja, A. (2010). The frequency of forest fires in Scots pine
1369 stands of Tuva, Russia. *Environmental Research Letters*, 5(1), 015002.

1370 Kang, Y., Choi, H., Im, J., Park, S., Shin, M., Song, C.-K., *et al.* (2021). Estimation of surface-level NO₂
1371 and O₃ concentrations using TROPOMI data and machine learning over East Asia.
1372 *Environmental Pollution*, 288, 117711.

1373 Kang, Y., Kim, M., Kang, E., Cho, D., & Im, J. (2022). Improved retrievals of aerosol optical depth and
1374 fine mode fraction from GOCI geostationary satellite data using machine learning over East
1375 Asia. *ISPRS Journal of Photogrammetry and Remote Sensing*, 183, 253-268.

1376 Karbowska, B., & Zembrzusi, W. (2016). Fractionation and mobility of thallium in volcanic ashes after
1377 eruption of Eyjafjallajökull (2010) in Iceland. *Bulletin of environmental contamination and*
1378 *toxicology*, 97, 37-43.

1379 Kaufman, Y. J., & Boucher, O. (2002). A satellite view of aerosols in the climate system. *Nature*,
1380 419(6903), 215-215.

1381 Kim, D. H., Sohn, B. J., Nakajima, T., Takamura, T., Takamura, T., Choi, B. C., *et al.* (2004). Aerosol
1382 optical properties over east Asia determined from ground-based sky radiation measurements.
1383 *Journal of Geophysical Research-Atmospheres*, 109(D2).

1384 King, M. D., Byrne, D. M., Herman, B. M., & Reagan, J. A. (1978). Aerosol Size Distributions Obtained
1385 by Inversions of Spectral Optical Depth Measurements. *Journal of the Atmospheric Sciences*,
1386 35(11).

1387 Klett, J. D. (1985). Lidar inversion with variable backscatter/extinction ratios. *Applied Optics*, 24(11),
1388 1638-1643.

1389 Klingmüller, K., Pozzer, A., Metzger, S., Stenchikov, G. L., & Lelieveld, J. (2016). Aerosol optical depth
1390 trend over the Middle East. *Atmospheric Chemistry and Physics*, 16(8), 5063-5073.

1391 Koelemeijer, R., Homan, C., & Matthijsen, J. (2006). Comparison of spatial and temporal variations of
1392 aerosol optical thickness and particulate matter over Europe. *Atmospheric Environment*, 40(27),
1393 5304-5315.

1394 Koschmieder, H. (1924). Theorie der horizontalen Sichtweite. *12*, 33-55.

1395 Krylov, A., McCarty, J. L., Potapov, P., Loboda, T., Tyukavina, A., Turubanova, S., *et al.* (2014). Remote
1396 sensing estimates of stand-replacement fires in Russia, 2002–2011. *Environmental Research*
1397 *Letters*, 9(10), 105007.

1398 Kulmala, M., Vehkamäki, H., Petäjä, T., Dal Maso, M., Lauri, A., Kerminen, V. M., *et al.* (2004).

1399 Formation and growth rates of ultrafine atmospheric particles: A review of observations.
1400 *Journal of Aerosol Science*, 35(2), 143-176.

1401 Kummu, M., De Moel, H., Salvucci, G., Viviroli, D., Ward, P. J., & Varis, O. (2016). Over the hills and
1402 further away from coast: global geospatial patterns of human and environment over the 20th–
1403 21st centuries. *Environmental Research Letters*, 11(3), 034010.

1404 Laj, P., Bigi, A., Rose, C., Andrews, E., Lund Myhre, C., Collaud Coen, M., *et al.* (2020). A global
1405 analysis of climate-relevant aerosol properties retrieved from the network of Global Atmosphere
1406 Watch (GAW) near-surface observatories. *Atmospheric Measurement Techniques*, 13(8), 4353–
1407 4392.

1408 Lapen, D. R., & Hayhoe, H. N. (2003). Spatial analysis of seasonal and annual temperature and
1409 precipitation normals in southern Ontario, Canada. *Journal of Great Lakes Research*, 29(4),
1410 529-544.

1411 Lee, L. A., Reddington, C. L., & Carslaw, K. S. (2016). On the relationship between aerosol model
1412 uncertainty and radiative forcing uncertainty. *Proceedings of the National Academy of Sciences*,
1413 113(21), 5820-5827.

1414 Levy, R. C., Mattoo, S., Munchak, L. A., Remer, L. A., Sayer, A. M., Patadia, F., *et al.* (2013). The
1415 Collection 6 MODIS aerosol products over land and ocean. *Atmospheric Measurement*
1416 *Techniques*, 6(11), 2989-3034.

1417 Levy, R. C., Mattoo, S., Sawyer, V., Shi, Y., Colarco, P. R., Lyapustin, A. I., *et al.* (2018). Exploring
1418 systematic offsets between aerosol products from the two MODIS sensors. *Atmospheric*
1419 *Measurement Techniques*, 11(7), 4073-4092.

1420 Levy, R. C., Remer, L. A., Mattoo, S., Vermote, E. F., & Kaufman, Y. J. (2007). Second-generation
1421 operational algorithm: Retrieval of aerosol properties over land from inversion of Moderate
1422 Resolution Imaging Spectroradiometer spectral reflectance. *Journal of Geophysical Research:*
1423 *Atmospheres*, 112(D13).

1424 Li, J., Carlson, B. E., Yung, Y. L., Lv, D., Hansen, J., Penner, J. E., *et al.* (2022). Scattering and absorbing
1425 aerosols in the climate system. *Nature Reviews Earth & Environment*, 3(6), 363-379.

1426 Li, J., Garshick, E., Hart, J. E., Li, L., Shi, L., Al-Hemoud, A., *et al.* (2021). Estimation of ambient PM2.5
1427 in Iraq and Kuwait from 2001 to 2018 using machine learning and remote sensing. *Environment*
1428 *International*, 151.

1429 Li, L. (2020). A robust deep learning approach for spatiotemporal estimation of satellite AOD and PM2.
1430 5. *Remote Sensing*, 12(2), 264.

1431 Li, S., Chen, L., Huang, G., Lin, J., Yan, Y., Ni, R., *et al.* (2020). Retrieval of surface PM2. 5 mass
1432 concentrations over North China using visibility measurements and GEOS-Chem simulations.
1433 *Atmospheric Environment*, 222, 117121.

1434 Li, Z., Lau, W. M., Ramanathan, V., Wu, G., Ding, Y., Manoj, M., *et al.* (2016). Aerosol and monsoon
1435 climate interactions over Asia. *Reviews of Geophysics*, 54(4), 866-929.

1436 Liao, H., Chang, W., & Yang, Y. (2015). Climatic Effects of Air Pollutants over China: A Review.
1437 *Advances in Atmospheric Sciences*, 32(1), 115-139.

1438 Lin, J. T., van Donkelaar, A., Xin, J. Y., Che, H. Z., & Wang, Y. S. (2014). Clear-sky aerosol optical depth
1439 over East China estimated from visibility measurements and chemical transport modeling.
1440 *Atmospheric Environment*, 95, 258-267.

1441 Liu, B., Ma, X., Ma, Y., Li, H., Jin, S., Fan, R., *et al.* (2022). The relationship between atmospheric
1442 boundary layer and temperature inversion layer and their aerosol capture capabilities.

1443 *Atmospheric Research*, 271.

1444 Mahowald, N. M., Ballantine, J. A., Feddema, J., & Ramankutty, N. (2007). Global trends in visibility:
1445 implications for dust sources. *Atmospheric Chemistry and Physics*, 7(12), 3309-3339.

1446 Marengo, F., Santacesaria, V., Bais, A. F., Balis, D., di Sarra, A., Papayannis, A., *et al.* (1997). Optical
1447 properties of tropospheric aerosols determined by lidar and spectrophotometric measurements
1448 (Photochemical Activity and Solar Ultraviolet Radiation campaign). *Applied Optics*, 36(27),
1449 6875-6886.

1450 McNeill, V. F. (2017). Atmospheric Aerosols: Clouds, Chemistry, and Climate. In J. M. Prausnitz (Ed.),
1451 *Annual Review of Chemical and Biomolecular Engineering, Vol 8* (Vol. 8, pp. 427-444).

1452 Mehta, M., Singh, R., Singh, A., & Singh, N. (2016). Recent global aerosol optical depth variations and
1453 trends—A comparative study using MODIS and MISR level 3 datasets. *Remote Sensing of
1454 Environment*, 181, 137-150.

1455 Mitra, R., Bajpai, A., & Biswas, K. (2023). ADASYN-assisted machine learning for phase prediction of
1456 high entropy carbides. *Computational Materials Science*, 223.

1457 Mortier, A., Gliß, J., Schulz, M., Aas, W., Andrews, E., Bian, H., *et al.* (2020). Evaluation of climate
1458 model aerosol trends with ground-based observations over the last 2 decades—an AeroCom and
1459 CMIP6 analysis. *Atmospheric Chemistry and Physics*, 20(21), 13355-13378.

1460 Mukkavilli, S., Prasad, A., Taylor, R., Huang, J., Mitchell, R., Troccoli, A., *et al.* (2019). Assessment of
1461 atmospheric aerosols from two reanalysis products over Australia. *Atmospheric Research*, 215,
1462 149-164.

1463 Nagaraja Rao, C., Stowe, L., & McClain, E. (1989). Remote sensing of aerosols over the oceans using
1464 AVHRR data Theory, practice and applications. *International Journal of Remote Sensing*, 10(4-
1465 5), 743-749.

1466 Nakajima, T., Campanelli, M., Che, H., Estellés, V., Irie, H., Kim, S.-W., *et al.* (2020). An overview of
1467 and issues with sky radiometer technology and SKYNET. *Atmospheric Measurement
1468 Techniques*, 13(8), 4195-4218.

1469 NOAA, DOD, FAA, & USN (1998). Automated Surface Observing System (ASOS) User's Guide.

1470 O'Reilly, J. E., Maritorena, S., Mitchell, B. G., Siegel, D. A., Carder, K. L., Garver, S. A., *et al.* (1998).
1471 Ocean color chlorophyll algorithms for SeaWiFS. *Journal of Geophysical Research-Oceans*,
1472 103(C11), 24937-24953.

1473 Pebesma, E. J. (2004). Multivariable geostatistics in S: the gstat package. *Computers & Geosciences*,
1474 30(7), 683-691.

1475 Prakash, P. J., Stenchikov, G., Kalenderski, S., Osipov, S., & Bangalath, H. (2014). The impact of dust
1476 storms on the Arabian Peninsula and the Red Sea. *Atmospheric Chemistry & Physics
1477 Discussions*, 14(13).

1478 Qiu, J. (1997). The method of wide-band remote atmospheric aerosol optical depth and its application
1479 (in Chinese). *J. Remote Sens.*, 1(1), 15-23.

1480 Qiu, J., & Lin, Y. (2001). A parameterization model of aerosol optical depths in China. *Acta
1481 Meteorologica Sinica*, 59(3), 368-372.

1482 Ramanathan, V., Crutzen, P. J., Kiehl, J., & Rosenfeld, D. (2001). Aerosols, climate, and the hydrological
1483 cycle. *Science*, 294(5549), 2119-2124.

1484 Remer, L. A., Kaufman, Y. J., Tanre, D., Mattoo, S., Chu, D. A., Martins, J. V., *et al.* (2005). The MODIS
1485 aerosol algorithm, products, and validation. *Journal of the Atmospheric Sciences*, 62(4), 947-
1486 973.

1487 Remer, L. A., Kleidman, R. G., Levy, R. C., Kaufman, Y. J., Tanre, D., Mattoo, S., *et al.* (2008). Global
1488 aerosol climatology from the MODIS satellite sensors. *Journal of Geophysical Research-*
1489 *Atmospheres*, 113(D14).

1490 Salomonson, V. V., Barnes, W. L., Maymon, P. W., Montgomery, H. E., & Ostrow, H. (1987). MODIS:
1491 advanced facility instrument for studies of the Earth as a system. *Geoscience & Remote Sensing*
1492 *IEEE Transactions on*, 27(2), 145-153.

1493 Sawamura, P., Vernier, J. P., Barnes, J. E., Berkoff, T. A., Welton, E. J., Alados-Arboledas, L., *et al.*
1494 (2012). Stratospheric AOD after the 2011 eruption of Nabro volcano measured by lidars over
1495 the Northern Hemisphere. *Environmental Research Letters*, 7(3), 34013-34021(34019).

1496 Schutgens, N., Tsyro, S., Gryspeerd, E., Goto, D., Weigum, N., Schulz, M., *et al.* (2017). On the spatio-
1497 temporal representativeness of observations. *Atmospheric Chemistry and Physics*, 17(16), 9761-
1498 9780.

1499 Singh, A., Mahata, K. S., Rupakheti, M., Junkermann, W., Panday, A. K., & Lawrence, M. G. (2019). An
1500 overview of airborne measurement in Nepal—Part 1: Vertical profile of aerosol size, number,
1501 spectral absorption, and meteorology. *Atmospheric Chemistry and Physics*, 19(1), 245-258.

1502 Smirnov, A., Holben, B., Slutsker, I., Giles, D., McClain, C., Eck, T., *et al.* (2009). Maritime aerosol
1503 network as a component of aerosol robotic network. *Journal of Geophysical Research:*
1504 *Atmospheres*, 114(D6).

1505 Steinberg, D., & Colla, P. (2009). CART: classification and regression trees. *The top ten algorithms in*
1506 *data mining*, 9, 179.

1507 Streets, D. G., Yan, F., Chin, M., Diehl, T., Mahowald, N., Schultz, M., *et al.* (2009). Anthropogenic and
1508 natural contributions to regional trends in aerosol optical depth, 1980–2006. *Journal of*
1509 *Geophysical Research: Atmospheres*, 114(D10).

1510 Sun, E., Xu, X., Che, H., Tang, Z., Gui, K., An, L., *et al.* (2019). Variation in MERRA-2 aerosol optical
1511 depth and absorption aerosol optical depth over China from 1980 to 2017. *Journal of*
1512 *Atmospheric and Solar-Terrestrial Physics*, 186, 8-19.

1513 Sun, Y., & Zhao, C. (2020). Influence of Saharan dust on the large-scale meteorological environment for
1514 development of tropical cyclone over North Atlantic Ocean Basin. *Journal of Geophysical*
1515 *Research: Atmospheres*, 125(23), e2020JD033454.

1516 Teixeira, A. (2004). Classification and regression tree. *Revue Des Maladies Respiratoires*, 21(6), 1174-
1517 1176.

1518 Tian, X., Tang, C., Wu, X., Yang, J., Zhao, F., & Liu, D. (2023). The global spatial-temporal distribution
1519 and EOF analysis of AOD based on MODIS data during 2003-2021. *Atmospheric Environment*,
1520 302.

1521 Tupper, A., Oswalt, J. S., & Rosenfeld, D. (2005). Satellite and radar analysis of the volcanic-
1522 cumulonimbi at Mount Pinatubo, Philippines, 1991. *Journal of Geophysical Research:*
1523 *Atmospheres*, 110(D9).

1524 Vasilyev, O., Contreras, A. L., Velazquez, A. M., Fabi, R. P. y., Ivlev, L., Kovalenko, A., *et al.* (1995).
1525 Spectral optical properties of the polluted atmosphere of Mexico City (spring-summer 1992).
1526 *Journal of Geophysical Research: Atmospheres*, 100(D12), 26027-26044.

1527 Vernier, J. P., Thomason, L. W., Pommereau, J. P., Bourassa, A., Pelon, J., Garnier, A., *et al.* (2011).
1528 Major influence of tropical volcanic eruptions on the stratospheric aerosol layer during the last
1529 decade. *Geophysical Research Letters*, 38(12).

1530 Wang, K., Dickinson, R. E., & Liang, S. (2009). Clear Sky Visibility Has Decreased over Land Globally

1531 from 1973 to 2007. *Science*, 323(5920), 1468-1470.

1532 Wang, K. C., Dickinson, R. E., Su, L., & Trenberth, K. E. (2012). Contrasting trends of mass and optical
1533 properties of aerosols over the Northern Hemisphere from 1992 to 2011. *Atmospheric Chemistry
1534 and Physics*, 12(19), 9387-9398.

1535 Wei, J., Li, Z., Peng, Y., & Sun, L. (2019a). MODIS Collection 6.1 aerosol optical depth products over
1536 land and ocean: validation and comparison. *Atmospheric Environment*, 201, 428-440.

1537 Wei, J., Li, Z., Sun, L., Peng, Y., Liu, L., He, L., et al. (2020). MODIS Collection 6.1 3 km resolution
1538 aerosol optical depth product: Global evaluation and uncertainty analysis. *Atmospheric
1539 Environment*, 240, 117768.

1540 Wei, J., Peng, Y., Guo, J., & Sun, L. (2019b). Performance of MODIS Collection 6.1 Level 3 aerosol
1541 products in spatial-temporal variations over land. *Atmospheric Environment*, 206, 30-44.

1542 Welton, E. J., Campbell, J. R., Berkoff, T. A., Spinhirne, J. D., & Starr, D. O. (2002). The micro-pulse
1543 lidar network (MPLNET).

1544 Winker, D. M., Tackett, J. L., Getzewich, B. J., Liu, Z., Vaughan, M. A., & Rogers, R. R. (2013). The
1545 global 3-D distribution of tropospheric aerosols as characterized by CALIOP. *Atmospheric
1546 Chemistry and Physics*, 13(6), 3345-3361.

1547 Winker, D. M., Vaughan, M. A., Omar, A., Hu, Y., Powell, K. A., Liu, Z., et al. (2009). Overview of the
1548 CALIPSO Mission and CALIOP Data Processing Algorithms. *Journal of Atmospheric and
1549 Oceanic Technology*, 26(11), 2310-2323.

1550 Wu, J., Luo, J., Zhang, L., Xia, L., Zhao, D., & Tang, J. (2014). Improvement of aerosol optical depth
1551 retrieval using visibility data in China during the past 50years. *Journal of Geophysical
1552 Research-Atmospheres*, 119(23), 13370-13387.

1553 Xia, X., Che, H., Zhu, J., Chen, H., Cong, Z., Deng, X., et al. (2016). Ground-based remote sensing of
1554 aerosol climatology in China: Aerosol optical properties, direct radiative effect and its
1555 parameterization. *Atmospheric Environment*, 124(JAN.PT.B), 243-251.

1556 Xie, Y., Wang, Y., Zhang, K., Dong, W., Lv, B., & Bai, Y. (2015). Daily estimation of ground-level PM_{2.5}
1557 concentrations over Beijing using 3 km resolution MODIS AOD. *Environmental Science &
1558 Technology*, 49(20), 12280-12288.

1559 Yang, X., Wang, Y., Zhao, C., Fan, H., Yang, Y., Chi, Y., et al. (2022). Health risk and disease burden
1560 attributable to long-term global fine-mode particles. *Chemosphere*, 287.

1561 Yang, X., Zhao, C., Yang, Y., & Fan, H. (2021a). Long-term multi-source data analysis about the
1562 characteristics of aerosol optical properties and types over Australia. *Atmospheric Chemistry
1563 and Physics*, 21(5), 3803-3825.

1564 Yang, X., Zhao, C., Yang, Y., Yan, X., & Fan, H. (2021b). Statistical aerosol properties associated with
1565 fire events from 2002 to 2019 and a case analysis in 2019 over Australia. *Atmospheric Chemistry
1566 and Physics*, 21(5), 3833-3853.

1567 Yang, Y., Ge, B., Chen, X., Yang, W., Wang, Z., Chen, H., et al. (2021c). Impact of water vapor content
1568 on visibility: Fog-haze conversion and its implications to pollution control. *Atmospheric
1569 Research*, 256.

1570 Yoon, J., Burrows, J., Vountas, M. v., von Hoyningen-Huene, W., Chang, D., Richter, A., et al. (2014).
1571 Changes in atmospheric aerosol loading retrieved from space-based measurements during the
1572 past decade. *Atmospheric Chemistry and Physics*, 14(13), 6881-6902.

1573 Yoon, J., Pozzer, A., Chang, D. Y., Lelieveld, J., Kim, J., Kim, M., et al. (2016). Trend estimates of
1574 AERONET-observed and model-simulated AOTs between 1993 and 2013. *Atmospheric*

1575 *Environment*, 125, 33-47.

1576 Zhang, S., Wu, J., Fan, W., Yang, Q., & Zhao, D. (2020). Review of aerosol optical depth retrieval using
1577 visibility data. *Earth-Science Reviews*, 200, 102986.

1578 Zhang, Z., Wu, W., Wei, J., Song, Y., Yan, X., Zhu, L., *et al.* (2017). Aerosol optical depth retrieval from
1579 visibility in China during 1973-2014. *Atmospheric Environment*, 171, 38-48.

1580 Zhao, A. D., Stevenson, D. S., & Bollasina, M. A. (2019). The role of anthropogenic aerosols in future
1581 precipitation extremes over the Asian Monsoon Region. *Climate Dynamics*, 52(9-10), 6257-
1582 6278.

1583 Ziemba, L. D., Lee Thornhill, K., Ferrare, R., Barrick, J., Beyersdorf, A. J., Chen, G., *et al.* (2013).
1584 Airborne observations of aerosol extinction by in situ and remote-sensing techniques:
1585 Evaluation of particle hygroscopicity. *Geophysical Research Letters*, 40(2), 417-422.

1586